Journal Name

ARTICLE

Low-Temperature Processed Non-TiO_2 Electron Selective Layers for Perovskite Solar Cells

Received 00th January 20xx,
Accepted 00th January 20xx

DOI: 10.1039/x0xx00000x

www.rsc.org/

Zhanglin Guo,[a] Liguo Gao,[b] Chu Zhang,[a] Zhenhua Xu,[a] Tingli Ma[a, b*]

Organic-inorganic halide perovskite solar cells (PSCs) have been paid much attention in recent years and their power conversion efficiency (PCE) has rapidly improved from 3.8% to 22.7%. However, the commonly used electron selective layer (ESL), TiO_2, requires a high-temperature post-treatment during its preparation process, which is not compatible with the flexible PSCs on the plastic substrates. Moreover, it is energy intensive and not suitable for the low-cost mass production of PSCs. Developing low-temperature processable ESLs can solve these problems and realize the all-low-temperature fabrication of PSCs. Therefore, in this review, the current progress in low-temperature processed ESLs, especially non-TiO_2 inorganic, organic materials and quantum dots (QDs), such as SnO_2, ZnO, WO_x, CeO_x, Nb_2O_5, In_2O_3, CdS, Bi_2S_3, In_2S_3, Zn_2SnO_4, fullerene, non-fullerene, CdSe QDs, etc., are summarized. Their preparation methods, properties and applications for use in PSCs are highlighted. Several results by our group are also introduced. These low-temperature processed ESLs will provide more possibilities for implementing the all-low-temperature fabrication of PSCs with high performances.

1. Introduction

Over the last decade, deploying solar cells photovoltaics is regarded as one of the most promising choices of replacing traditional fossil fuels. Among the various photovoltaic devices, PSCs experienced the highest speed increase in PCE over the past seven years.[1, 2] Currently, perovskite photovoltaic devices exhibit a PCE as high as 22.7%, comparable to the more established thin-film inorganic photovoltaics such as copper indium gallium selenide (CIGS) and cadmium telluride (CdTe) solar cells.[2] More importantly, PSCs are low-temperature processable, which results in the significant advantage for next-generation cost-competitive photovoltaic technology to address the scalability issue. Meanwhile, the low-temperature solution processability makes PSCs compatible with the flexible and wearable electrical devices.[3, 4]

A typical PSC is comprised of five parts as shown in Fig. 1a. They are the front electrode of a transparent conductive oxide (mainly fluorine-doped tin oxide (FTO) or indium tin oxide (ITO)) on the rigid or flexible substrate, ESL, perovskite layer, hole transporting layer (HTL), and back electrode of a noble metal, carbon or metal oxide.[5, 6] The ESL is designed to collect and transport the photogenerated electrons and block the holes from the perovskite, while the HTL has the role of transporting holes and blocking electrons from the perovskite. Due to the ambipolar property of the perovskite light absorber, the transportation mechanism efficiently works. The perovskite light absorber, with the formula of ABX_3 (A=CH_3NH_3 (abbreviated as MA), $HC(NH_2)_2$ (abbreviated as FA), Cs; B=Pb, Sn; X=Cl, Br, I), is the core of the PSCs. The advantages of the perovskite include a suitable bandgap, high absorption coefficient, and long carrier transport distance that account for the high performances of the PSCs.[7] The most widely used HTL is the organic p-type semiconductor of 2,2',7,7'-tetrakis[N,N-di(4-methoxyphenyl)amino]-9,9'-spirobifluorene (Spiro-MeOTAD). In addition, some other p-type materials, such as Poly(3-hexylthiophene-2,5-diyl) (P3HT), Poly[bis(4-phenyl)(2,4,6-trimethylphenyl)amine (PTAA), NiO, CuSCN, and $CuGaO_2$, have also been utilized as efficient HTLs.[8]

In the structure of the PSCs, the perovskite material can absorb light over a broad spectral range owing to its narrow band gap and effectively convert the incident light into charges.[9] The photogenerated electrons and holes coexist in perovskite layer due to its unique ambipolar property.[10, 11] Then the electrons can be injected into the n-type ESL (with subsequent electron transport to the FTO electrode) and holes can be transferred to the p-type HTL (with subsequent transport to the Au electrode), as shown in Fig. 1b. Additionally, the ESL performs as an electron blocking layer to prevent the holes from the perovskite and HTL from reaching the FTO electrode due to its valance band position is lower than that of the perovskite materials. Meanwhile, the HTL blocks the electrons from the perovskite and ESL due to its higher conduction band position than that of the perovskite materials. Therefore, the effectively charge transportation and blocking mechanism can avoid the short circuit in the device. The uniform films including the ESL, the perovskite layer and the HTL, and the optimized interfaces are crucial to the performance of the PSCs.

TiO_2 is commonly used as ESL materials in most PSCs. Despite the excellent PCEs, high temperature (around 500 °C) post-treatment of the TiO_2 layer is always necessary in order get a condensed TiO_2 layer with a high crystallinity and conductivity.[12] The high temperature hinders the simple and low cost mass production of PSCs, because the annealing is complex and energy intensive.

[a] Graduate School of Life Science and Systems Engineering, Kyushu Institute of Technology, Kitakyushu, Fukuoka 808-0196, Japan.
[b] School of Petroleum and Chemical Engineering, Dalian University of Technology, Panjin Campus, Panjin 124221, P. R. China.
* E-mail: tinglima@life.kyutech.ac.jp (Prof. Tingli Ma)

Moreover, PSCs based on TiO_2 are suffering from UV-light instability due to the high photocatalytic activity of the TiO_2, which can damage the perovskite materials and impede the reproducibility of the devices.[13, 14] Another drawback of the TiO_2 is that the electron mobility (1 $cm^2V^{-1}s^{-1}$) is much lower than that of the perovskite layer (24.8 1 $cm^2V^{-1}s^{-1}$), resulting in an unbalanced charge transport.[15] The imperfect alignment between the conduction bands of TiO_2 and the perovskite layer, resulting in hysteresis of the J-V characteristic, might be another disadvantage. Therefore, considerable attention has been devoted to modify the conventional TiO_2 ESL in order to overcome the aforementioned disadvantages. The general strategies are preparing low-temperature processable amorphous TiO_x film,[16] constructing TiO_2 composite film with other compounds,[17, 18] morphology controlling of the TiO_2 film,[19] and metals doping within the TiO_2 film.[20-22] For instance, Ta doped TiO_2 ESL based PSCs exhibited remarkable improvement in PCE, as compared to those with un-doped TiO_2 .[21, 22]

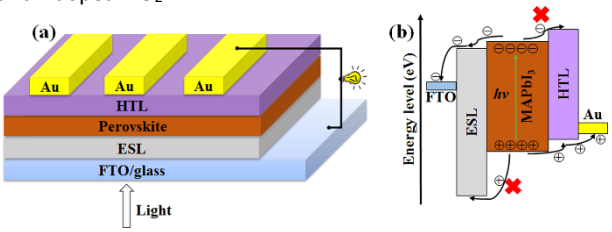

Fig. 1 (a) Schematic view and (b) the working mechanism of PSCs.

Flexible PSCs are fabricated on flexible substrates, such as polyethylene naphthalate/indium-doped tin oxide (PEN/ITO)-coated substrates, the ethylene terephthalate/indium-doped tin oxide (PET/ITO)-coated substrates, etc.[23-26] These flexible PSCs have great potential of being used in wearable electrical devices because they can maintain a high performance even after being bent for thousands of times during use.[24] Meanwhile, these flexible substrates are low-cost and lightweight, benefiting for the commercialization of wearable electronics. However, different from the rigid substrates including glass/FTO and glass/ITO, these flexible substrates are not able to withstand high temperatures. Therefore, low-temperature processable ESLs are urgently required for manufacturing high-performance flexible PSCs, which will promote the industrial printing processes with roll-to-roll technology and reducing the production costs of wearable electronics.

Inspired by the low-temperature fabrication of the perovskite layer and the HTL, it is crucial to develop efficient and low-temperature processable ESLs to reduce the production costs, simplify the process, meet the requirement for flexible PSCs fabrication, and realize the all-low-temperature mass manufacturing of the PSCs.

Therefore, many groups have been focusing on developing low-temperature processed non-TiO_2 ESL materials, such as inorganic materials, organic materials and QDs. Their target is to simplify the preparation process and further improve the performances of the PSCs. Although reviews have reported the progress of n-type semiconductors in PSCs, none of them has focused on the development of low-temperature processable non-TiO_2 ESLs.[27-29] We now summarize the recent advancements in low-temperature processed non-TiO_2 ESLs, encompassing their preparation, properties, and applications in PSCs. We also discuss the issues in further developments of the low-temperature ESLs.

2. Inorganic ESLs

2.1 Binary metal compound ESLs

2.1.1 SnO_2 ESLs

Tin oxide (SnO_2) is regarded as an ideal alternative material for the TiO_2 ESL. SnO_2 has a large band gap of 3.6-3.8 eV, which results in a high transparency throughout the visible region and the proper band structure makes it possess the ability to transport electrons and block the holes. At the same time, SnO_2 displays a carrier mobility about two orders of magnitude higher than that of TiO_2. Our group has done some research on the SnO_2-based PSCs, in which the high-temperature sintering was conducted as the first reported by Ma et al.[30-32] As for the low-temperature processes, Fang et al. first reported the PSCs based on the SnO_2 ESL with high PCEs in early 2015.[33] The SnO_2 ESLs were synthesized by spin-coating the $SnCl_2{\cdot}2H_2O$ precursor prepared at room temperature, following thermal annealing in air at 180 °C for 1 h. It was found that the FTO substrate coated with a 60-nm thick SnO_2 film has a high transmittance, even better than that of the bare FTO substrates. This is due to the antireflection effect of the SnO_2 film, which benefits the light transmission through the ESL and light absorption by the perovskite layer. A schematic view of the planar cell structure and the energy band diagram of the PSCs based on SnO_2 are shown in Fig. 2a and b, respectively. It was demonstrated that the low-temperature solution processed SnO_2 is an excellent ESL and the PSCs based on SnO_2 achieved high average PCEs of 16.44% and a superior efficiency of 17.21%. The remarkable performance of the PSCs originates from the good antireflection, high electron mobility and wide band gap of the SnO_2 nanocrystal film. Later in 2016, Hagfeldt and co-workers reported the highest PCE of close to 21% for the SnO_2-based PSCs.[34] They combined spin-coating and chemical bath deposition (SC-CBD) at a low temperature, as shown in Fig. 2c and d. Moreover, the perovskite layers grown on the prepared SnO_2 are composed of large crystals ca. 300 nm, indicating high quality perovskite layer.

Although the high efficiencies of the SnO_2-based PSCs have been achieved by a simple method, the high preparation temperature of SnO_2 limited its application to flexible PSCs. In order to decrease the fabrication temperature, Tietze et al. prepared an amorphous SnO_2 film by the CBD method at 55 °C without a post annealing treatment,[35] as shown in Fig. 2e. The results indicated that even when prepared under a very low temperature, the amorphous SnO_2 ESL possesses a high transparency and uniform substrate coverage. It acquired a perfect alignment of the conduction band at the SnO_2/$MAPbI_3$ interface, which can efficiently extract electrons, while the deep valence band of SnO_2 ensures a strong hole-blocking property.

Besides the spin-coating and CBD process, another direct deposition method, the dual-fuel combustion process was also employed by Jen et al.[36] In their research, the dual fuels were used to modulate the associated exothermic process of the combustion reaction and the homogeneous SnO_2 film was obtained at 140 °C. Perovskite film grown on the SnO_2 film exhibits a fully covered surface morphology with densely packed grains, whose average grain size is around 100-200 nm. The maximum PCE of 12.93% was achieved based on the single component SnO_2 ESL while the higher PCE of 15.18% with negligible hysteresis was acquired when passivated with a fullerene-based self-assembled monolayer (C60-SAM). Moreover, Jen's group also adopted the electrodeposition method to prepare the SnO_2 film.[37] During the electrodeposition process at the reaction temperature of 70 °C, they precisely

controlled the growth of the SnO_2 nanostructures, leading to an excellent adhesion between the SnO_2 layer and the substrate. With a high transparency, crystallinity, conductivity and the significant charge-extracting capability of the SnO_2 film, a PCE of 13.88% was achieved. More recently, Yan et al. used a plasma-enhanced atomic layer deposition method to prepare the SnO_2 film,[38] with a water vapor post treatment at 100 °C. They found that the water vapor treatment can improve the electrical conductivity. This is because annealing with water vapor facilitates the complete reaction of the organic materials, leading to the formation of a purer SnO_2. With this SnO_2 ESL, they achieved a very high PCE of 18.36% on the flexible substrate, which is the highest among the flexible PSCs with a regular structure.

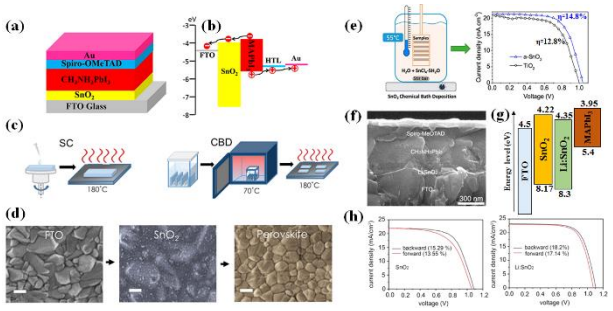

Fig. 2 (a) Schematic view and (b) Energy band diagram of the SnO_2 ESL based PSCs structure.[33] (c) Schematic illustration of SC-CBD method and (d) Top-view scanning electron microscopy (SEM) images of the low-temperature layer by layer deposition process: Bare FTO, SnO_2 deposited by SC-CBD process on FTO and the perovskite crystals grown atop.[34] (e) Schematic illustration of chemical bath deposition method and J-V curves of the PSCs with a-SnO_2 or compact TiO_2 as ESL.[35] (f) Cross-sectional SEM image, (g) Energy diagram and (h) J-V curves measured at backward-forward scan of the PSCs with the Li:SnO_2 as ESL.[39] Adapted with permission from ref. 33, 34, 35 and 39. Copyright 2015 American Chemical Society, 2016 The Royal Society of Chemistry, 2017 American Chemical Society, 2016 Elsevier.

Spin-coating of pre-synthesized nanocrystals on the substrate with a subsequent heat treatment was reported by Wang and co-workers.[40] They spin-coated the purchased SnO_2 nanoparticles (ca. 22-43 nm) and baked them at 200 °C for 1 h. The SnO_2-based PSCs with the passivation of the SnO_2/perovskite interface by the remnant PbI_2 crystallites achieved the maximum PCE of 13.0% with an excellent durability. Their results also indicate that the reduction of photovoltaic performance upon light illumination of the PSC devices is not attributed to the degradation of materials, but is resulted from the ferroelectric nature of the perovskite materials that accumulate charge carriers at the interface to interfere with the electricity flow at the working conditions. Lately, Zhang et al.[41] did a similar study by directly spin-coating the purchased SnO_2 nanoparticles, then subsequently baking at 150 °C for 30 min. With the $HC(NH_2)_2PbI_3$ based perovskite absorber, the SnO_2 based devices are almost free of hysteresis because of the enhanced electron extraction from the perovskite to SnO_2 and no obvious charge accumulation at the interface. In addition, perovskite films grown on SnO_2 and TiO_2 displayed similar crystal morphologies and thicknesses. Thus, the different hysteresis behaviours mainly originate from the different ESLs and the SnO_2 is a better ESL especially in the electron transportation property. The high PCE of 20.27% for SnO_2 based PSCs was obtained after introducing a PbI_2 passivation phase.

Even though high PCEs of over 20% have already been achieved, some researchers pointed out that the hysteresis behaviour of the SnO_2-based planar PSCs can be reduced by further improve the electron extraction efficiency across the interface.[39, 42, 43] Therefore, researchers doped metal into the SnO_2. For example, Ko et al. prepared an effective Li:SnO_2 ESL by a spin-coating process and post annealing at 185 °C.[39] The doped Li in the SnO_2 enhanced the conductivity and induced a downward shift of the conduction band minimum of the SnO_2, which facilitated the injection and transfer of electrons from the conduction band of the perovskite (Fig. 2f and g). Highly crystalline and pin hole-free perovskite films were prepared on both SnO_2 and Li:SnO_2 film and there were no obvious differences. The PCE was found to be 18.2% and 14.78% for the rigid and flexible substrates, respectively (Fig. 2h). Huang et al.[42] prepared the Sb-doped SnO_2 nanocrystallines by a precipitation method, then spin-coated them on the substrate with further annealing at 100 °C. They found that doping with Sb could increase the electrical conductivity and improve the Fermi level of the SnO_2, which in turn, improved the FF and the Voc of the devices. The PCE of devices was improved from 15.7 to 17.7 % with reduced hysteresis after Sb doping. More recently, Yan et al.[44] prepared Y-doped SnO_2 nanosheet arrays by an in situ hydrothermal growth process at 95 °C. They found that the Y-doped SnO_2 induced a more positive conduction band position than the undoped SnO_2 and the nanosheet arrays improved the perovskite infiltration and enhanced the contact with the perovskite. While there were no significant morphological difference between the perovskite layer grown on doped and pristine SnO_2 layer. As a result, PSCs with the Y-SnO_2 ESL exhibited significantly improved PCEs of 17.29% with a much reduced hysteresis. Moreover, the Nb-doped SnO_2 ESL has also been studied.[45] Compared to the pristine SnO_2, the PCE of PSCs based on the Nb-doped SnO_2 ESL displayed the higher PCE of 17.57% than that of 15.13% for the pristine SnO_2-based PSCs. Fang et al.[46] incorporated a MgO nanolayer between the FTO electrode and SnO_2 ESL that enhanced the electron transporting and hole blocking properties, and the resultant PSCs displayed the high PCE of 18.23%. Moreover, SnO_2 was also composited with other materials,[43, 47, 48] such as phenyl-C61-butyric acid methyl ester (PCBM), C60 and graphene QDs, and high PCEs were achieved. From the reviewed literature, we found that no significant differences from the morphologies of the perovskite grown on SnO_2 and metal doped SnO_2. While metal doping into SnO_2 can improve the conductivity of the SnO_2 and modulate the band alignment in order to achieve a balance between the electron injection efficiency and the theoretical Voc of the devices.

Therefore, SnO_2 is a good candidate for a highly efficient ESL due to its excellent high conductivity. The low-temperature processes, such as spin-coating, chemical bath deposition and electrodeposition are promising methods to prepare dense SnO_2 films. Furthermore, doping SnO_2 with metals can properly modify the conduction band position and enhance the performance of the devices.

2.1.2 ZnO ESLs

ZnO is a kind of widely used n-type semiconductor with low cost and outstanding compatible properties. More importantly, due to its comparable energy structure and higher electron mobility, ZnO is regarded as a viable alternative to TiO_2 as an efficient ESL in PSCs. Actually, ZnO has been studied since 2013, in which the ZnO layers were prepared by a low-temperature solution process and the corresponding PSCs achieved high PCEs.[49-52] For example, Boix et al. prepared a ZnO compact layer by electrodeposition and ZnO nanorods layer by chemical bath deposition.[49] The PSCs on both rigid and flexible substrates were fabricated and the PCEs of 8.9% and 2.62% were achieved, respectively.

Kelly et al. prepared ZnO nanoparticles by a solution process, then spin-coated them on the substrate without post annealing.[53] They fabricated planar PSCs with the architecture and energy levels depicted in Fig 3a and b. Without a mesoporous layer, the growing of perovskite crystal growth was relatively unconstrained, with the formation of large crystals, which served to increase the carrier mobility, reduce recombination from defect and trap states and increase the effective optical path length of the device. Consequently, the PSCs on the rigid substrate exhibited the high PCE of 15.7% and a decent PCE of 10.2% for the flexible substrate (Fig. 3c). Subsequently, research of the ZnO ESL focused on modifying the surface morphology and simplifying the process.[54-57] Recently, Pelicano et al. developed a novel method by the oxidation of a Zn thin film in water to produce a ZnO film.[54] By varying the water temperature and growth time, they obtained various morphologies, such as particles, fibers, rods, tubes and platelets, with different preferential growth orientations.

The rod-like ZnO enables better perovskite penetration and effective interfacial area, which resulted in reduced charge carrier path length and increased photovoltaic parameters. While the PCEs of the ZnO-based PSCs were rather low (highest PCE of 5.96%), which was attributed to the additional factors, such as a large amount of pinholes in ZnO and high recombination possibility in the interface. Our group first prepared carbon-based planar PSCs on FTO glass and flexible polymer substrates with ZnO ESL,[56] and the energy level diagram is shown in Fig. 3d. The ZnO layer was prepared by direct spin-coating ZnO nanoparticles along with low-temperature drying. For the rigid and flexible PSCs, the PCE of 8% and 4% were achieved, respectively. The flexible devices were capable of maintaining 80% of their initial PCEs after 1000 times of bending. For the low-temperature solution processed ZnO films, there is a large amount of hydroxyl groups and defects on the film surface, which can reduce the PCEs and limit the long-time stability.[58, 59] Therefore, researchers also focused on modification of the ZnO surface or adding a buffer layer between the perovskite and ZnO. Lee and his co-workers [55] reported an effective surface modification method for the ZnO ESL, in which they combined UV exposure and nitric acid treatment to remove the hydroxyl group and passivate the surface defects in the ZnO film. The perovskite grown on the modified ZnO possess less pinholes and higher crystalline than those with only as-synthesized ZnO film. Therefore, after the surface modification, the PCE was increased to 14% and the stability of the PSCs was also enhanced compared to the pristine ZnO-based PSCs.

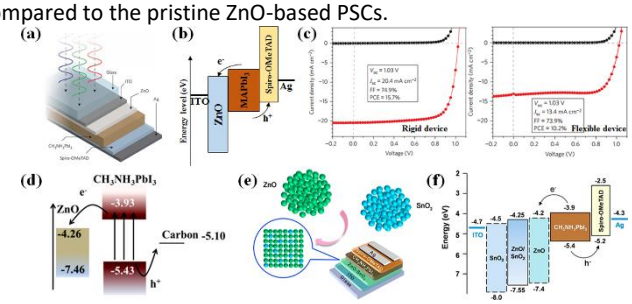

Fig. 3 (a) Device architecture, (b) Energy levels and (c) J-V curves of the ZnO ESL based PSCs on rigid and flexible substrate, respectively.[53] (d) Energy levels diagram of the ZnO ESL based PSCs with carbon electrode.[56] (e) Device architecture and (f) Energy level diagram of the PSCs based on ZnO, SnO_2 or ZnO/SnO_2 (2:1).[57] Adapted with permission from ref. 53, 56, and 57. Copyright 2014 Nature Publishing Group, 2015 American Chemical Society, 2016 Elsevier.

As for ZnO based nanocomposite ESL, Wang et al. prepared ZnO-SnO_2 nanocomposites with different Zn/Sn ratios at low temperature as the ESL for planar PSCs,[57] as shown in Fig. 3e. The nanocomposite with the optimal 89 mol% ZnO content displayed the highest PCE of 14.0%. Measurements showed that the ZnO-SnO_2 ESL possessed an excellent charge extraction efficiency and a large recombination resistance between the perovskite and ZnO-SnO_2, which were the main reasons for the higher performance than that of the single component ZnO and SnO_2 (Fig. 3f). Moreover, the ZnO-SnO_2 film-based PSCs exhibited better thermal stabilities than that of the ZnO-based PSCs, suggesting that the hydroxyl-induced degradation of the perovskite was predominant.

The ZnO-based PSCs have achieved high PCEs, while the stability of the device and the chemical stability of the ZnO are still important issues. The stability can be improved by surface modification, introducing buffer layers or constructing ZnO-based nanocomposite ESLs, which can optimize the interface between the perovskite and ZnO.

2.1.3 WO_x ESLs

Tungsten oxides (WO_x) are low-cost n-type semiconductors with suitable bandgaps (2 to 3 eV) and high electron mobility (10-20 $cm^2V^{-1}s^{-1}$). Recently, WO_x was used in PSCs as a component of the WO_x-TiO_2 core-shell nanostructure ESL,[60] while the ESL was prepared by a high temperature process. In early 2015, we first reported the low-temperature processed WO_x ESL based efficient PSCs.[61] As shown in Fig. 4a, the WO_x film was prepared using a facile spin-coating process and post heat-treatment at the low temperature of 150 °C. The results indicated that the WO_x film exhibited a comparable light transmittance but higher electrical conductivity than that of TiO_2 film. The perovskite grown on the WO_x had an oriented crystallization along ⟨110⟩ direction, which was not observed for the TiO_2 based sample. The orientation resulted in higher light absorption ability and faster electron extraction than those of the TiO_2 based device. Moreover, PSC based on the WO_x ESL exhibited a comparable PCE, higher short-circuit current density, but lower open-circuit voltage when compared to the TiO_2-based device. We found that for the WO_x-based PSCs, the poor Voc and FF were caused by the inherent charge recombination. In order to overcome this defect, we also first prepared a series of amorphous TiO_x-WO_x composite ESLs at the low temperatures of 150, 70 °C or even room temperature.[62] These amorphous WO_x based ESLs displayed an improved light transmittance, electrical conductivity, charge dissociation, and obviously suppressed charge recombination. After optimizing the ESL component prepared at 150 °C, the PSC achieved the high PCE of 14.47%. Meanwhile, PSCs with ESLs fabricated at 70 °C and room temperature were also very efficient with the maximum PCEs of 13.45% and 11.56%, respectively (Fig. 4b).

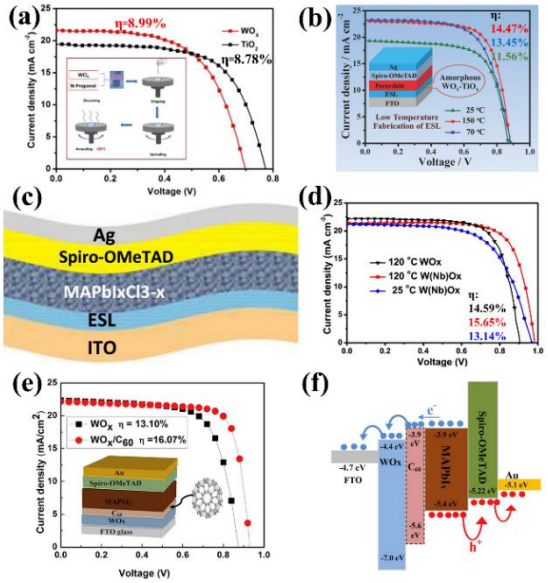

Fig. 4 (a) J-V curves of PSCs based on WO_x or TiO_2 (inset: spin-coating process of WO_x preparation).[61] (b) J-V curves of the champion PSCs based on WO_x-TiO_x composite ESL prepared at different temperatures (inset: device architecture of the PSCs).[62] (c) Configuration and (d) J-V curves of champion flexible PSCs based on W(Nb)Ox obtained under different temperatures.[63] (e) J-V curves (inset: configuration) and (f) Energy levels diagram of WO_x based PSCs.[64] Adapted with permission from ref. 61, 62, 63 and 64. Copyright 2015 American Chemical Society, 2016 Wiley, 2017 Elsevier, 2017 Elsevier.

As mentioned in the introduction, one of the most important reasons for developing low-temperature processed ESLs is to use them in flexible PSCs, in which the plastic substrate cannot withstand high temperatures. Therefore, we developed a series of niobium-modified tungsten oxides W(Nb)O_x ESLs on a plastic substrate at 120 °C and room temperature,[63] as shown in Fig. 4c. This is the first report on the metal doping in WO_x ESL. We found that modification with Nb^{5+} ions improved the electron transport ability of the WO_x-based ESL by enhancing the donor density, reducing the interfacial depletion width of the ITO/ESL, and minimizing the trap states of the ESL. The existence of capacitance C_E across the ESL in the ITO/ESL/perovskite structure could well interpret the effect of the ESL thickness on the hysteresis behaviour. The high PCEs of 15.65% and 13.14% were achieved with ESLs prepared at 120 °C and room temperature, respectively (Fig. 4d). Thus the amorphous and composite WO_x ESLs are very suitable for flexible PSCs with a high efficiency and low cost.

Gheno et al. compared the performance and stability of the WO_3-based PSCs to those of the classical PSC with a compact TiO_x and mesoporous TiO_2 layer.[65] In their research, the WO_3 ESLs were spin-coated or printed the WO_3 nanocrystals, with or without the post annealing process at 100 °C. The PCEs of the WO_3 ESL-based PSCs reached 9.5% for both the spin coating and print processes, lower than that the TiO_2-based PSCs of 15%. Moreover, they found that the WO_3 devices are more sensitive to moisture during illumination than the TiO_2 devices, leading to a decreased photocurrent, which is due to the higher photocatalytic property of the WO_3 than that of TiO_2. Under dark and ambient conditions, the WO_3 devices displayed an enhanced stability. Thus, the relatively small bandgap of the tungsten oxides (2-3 eV) has some negative effects on the stability of the devices because of the strong photocatalytic activities. In another study, Mori et al.[64] reported the highest PCE of the WO_x-based PSCs, in which they combined WO_x with C60 and achieved the high PCE of 16.07% (Fig. 4e). Characterizations suggested that the significantly improved efficiency by the WO_x/C60-based device originated from improved electron extraction, transportation and reduced charge recombination at the WO_x/C60 and perovskite interface (Fig. 4f).

Therefore, we think that the tungsten oxide can be a potential ESL candidate, especially for flexible devices. Some modifications should be conducted on the WO_x ESL for restraining the high photocatalytic activity to improve the device stability.

2.1.4 Other binary metal oxide ESLs

Besides the metal oxides summarized above, in the last two years, some other low-temperature processed metal oxides have also been prepared and used as the ESL for high performance PSCs.

Cerium oxide (CeO_x), with the merits of a wide band gap, high ionic conductivity, and high thermal and chemical stabilities, has a significant potential for use as an ESL in the PSCs. In 2017, Deng and co-workers prepared CeO_x through a simple sol-gel method at low temperature (150 °C) and applied into PSCs.[66] The configuration and the energy levels of the PSCs are shown in Fig. 5a and b. After optimizing by adjusting the precursor solution, they achieved the highest PCE of 14.32% for a single component CeO_x ESL. By introducing a thin PCBM layer between the CeO_x film and the perovskite layer, the PCE of the CeO_x-based PSCs increased to 17.04% (Fig. 5c). Moreover, the CeO_x-based devices exhibited a superior stability under light soaking, which might be attributed to the PCBM buffer layer by preventing the perovskite film from direct contact with the ESL. CeO_x might be a potential replacement for the high-temperature TiO_2 for PSCs, but the overall production cost would be another issue to be addressed.

Niobium oxide (Nb_2O_5) is an n-type semiconductor with a similar optical band structure, electronic properties and higher chemical stability relative to that of TiO_2. Miyasaka et al. reported the application of the Nb_2O_5 as a hole-blocking layer in the PSCs, but the thick Nb_2O_5 layer required a high-temperature (~500 °C) heat treatment.[67] Recently, researchers developed low-temperature processes to prepare the Nb_2O_5 films and they found that even when obtained at a low temperature, the Nb_2O_5 films still displayed a high conductivity and a suitable Fermi level for efficient electron extraction from the perovskite. For example, Liu's group developed an e-beam evaporation method to deposit the Nb_2O_5 film, which was directly used as an ESL without post-treatment.[68] Electrical impedance spectroscopy was performed to investigate the interfacial dynamics of the perovskite solar cells. Results indicated that the device based on Nb_2O_5 with 60 nm thickness exhibits the largest recombination resistance, indicating smallest carrier recombination processes. With the optimized ESL thickness, the PSCs fabricated on glass and PET substrate achieved the efficiency of 18.59% and 15.56%, respectively. Moreover, the e-beam evaporated Nb_2O_5 was found to be advantageous in large area flexible PSCs, with comparable Jsc and Voc values to smaller area devices, and the PCE loss was mainly caused by an increased series resistance leading to a reduced FF. They pointed out that further reducing the intrinsic

resistance of the devices should be an effective way to increase the FF and PCEs of both large-scale and flexible PSCs. Lately, the same group prepared a dense amorphous Nb_2O_5 via the room-temperature radio frequency magnetron sputtering technique.[69] The structure and energy level diagram are shown in Fig. 5d and e, respectively. Without heat treatment, the PSCs with this ESL achieved the highest PCE of 17.1% (Fig. 5d). Moreover, flexible PSCs based on the amorphous Nb_2O_5 also acquired the decent PCE of 12.1%.

Feng and co-workers reported another low-temperature method for Nb_2O_5 preparation.[70] Ultra small Nb_2O_5 nanoparticles were synthesized by a hydrolysis reaction using an ethanol-based $NbCl_5$ precursor and H_2O_2 as a strong oxidizer with UV treatment. The Nb_2O_5 nanoparticles were then spin-coated on FTO and used as the ESL of the PSCs. The peak PCE of the Nb_2O_5-based PSCs was 14.6%, which should be attributed to the high-transmittance, low capacitance and low series resistance of the Nb_2O_5 layer. Furthermore, the hysteresis was suppressed due to the increased conductivity and decreased capacitance of the Nb_2O_5. Therefore, Nb_2O_5 with excellent properties, low cost and low-temperature processing, has a great potential for replacing the high-temperature TiO_2 ESL.

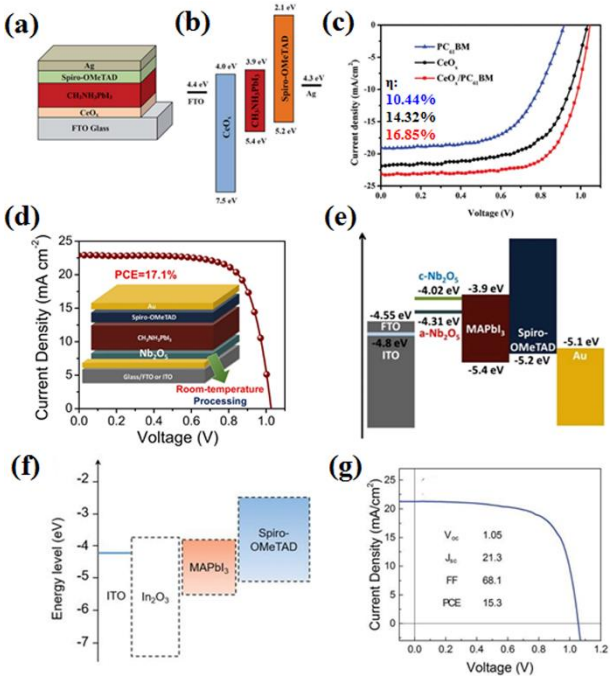

Fig. 5 (a) Device architecture, (b) Energy levels diagram and (c) J-V curves of CeO_x based PSCs.[66] (d) J-V curve (inset: device architecture) and (e) energy levels diagram of Nb_2O_5 based PSCs.[69] (f) Energy levels diagram and (g) J-V curve of In_2O_3 based PSCs.[71] Adapted with permission from ref. 66, 69 and 71. Copyright 2017 The Royal Society of Chemistry, 2017 American Chemical Society, 2017 The Royal Society of Chemistry.

Indium oxide (In_2O_3) is an n-type semiconductor with not only a wide band gap (~3.75 eV), but also a high mobility (~20 $cm^2V^{-1}s^{-1}$) and good thermal stability. These merits imply that In_2O_3 is a potential ESL candidate in PSCs. Recently, Fang et al.[72] first reported low-temperature sol-gel processed In_2O_3 films as ESLs in PSCs, and a PCE of 13.01% was obtained after optimizing the concentration of the precursor solution and the annealing temperature (200 °C is the most suitable). The In_2O_3 films exhibited a good antireflection property, leading to better light absorption by the perovskite layer. Furthermore, they improved the PCE of the In_2O_3-based PSCs to 14.83% after introducing a PCBM layer between the In_2O_3 ESL and the perovskite layer. Yin and co-workers did similar research with a different precursor and higher PCEs of 15.30% and steady-state efficiency of 14.39% were achieved,[71] as shown in Fig. 5f and g. After storage in the dark for three months, the PCE of the unsealed PSCs based on the In_2O_3 films retained 94% of their peak efficiency.

Therefore, we can conclude that many kinds of binary metal oxides with low-temperature process possibilities are potential alternatives of the currently used TiO_2 ESL. These low-temperature processed non-TiO_2 binary metal oxide ESLs can reduce the cost, simplify the fabrication process and provide more choices of ESL for PSCs.

2.1.5 CdS ESLs

Cadmium sulfide (CdS) is one of the most common metal chalcogenide materials due to its excellent stability and high mobility. CdS has been widely used in established CdTe and CIGS solar cells with an excellent stability and high mobility. It is reported that CdS has a comparable electron mobility and similar conduction band position to that of TiO_2.[73] Moreover, CdS is very easy to prepare by chemical bath deposition or a hydrothermal process.

Liu and co-workers introduced two metal sulfides as the ESL for PSCs.[74] After evaluating the alignment of the energy levels at the perovskite/metal sulfide interface, they found that the ZnS is not a proper ESL because its conduction band is higher than that of the perovskite (Fig. 6a and b). The CdS-based PSCs achieved a maximum PCE of 11.2% (Fig. 6c). They concluded that the proper conduction band offset at the interface for efficient electron collection and reduced recombination are the main reasons for the excellent performance of the CdS-based PSCs. The PCE of the CdS-based PSCs was recently further improved by Peng et al.[75] They prepared the CdS film by a chemical bath deposition process and the corresponding PSCs achieved the highest PCE so far of 16.1%, comparable to the TiO_2 PSCs. They proposed similar mechanisms that the CdS-based device presents a higher recombination resistance than the TiO_2-based devices, which reduces the carrier recombination and increases the open circuit voltage. The interface between the CdS and perovskite displayed an efficient carrier extraction and reduced the surface defect-associated degradation in the devices, which helped to alleviate the anomalous hysteresis and long-term instability. Gobbo's group then achieved a PCE of 11% for PSCs with the CdS ESL prepared by the chemical bath deposition process.[73] Moreover, they found that the device performance could be further improved through device optimization by controlling the interface and band gap tuning of the CdS by the doping method.

In another study, the thermal evaporation process was adopted by Yong et al. to prepare the CdS ESL for the planar PSCs.[76] The PSCs achieved the highest PCE of 12.2% (Fig. 6d) and the device displayed a considerably enhanced stability under continuous sunlight illumination (maintained 91% of its initial PCE after a 12-hour illumination). They attributed this great photo-stability to the advantageous characteristic of the oxygen-vacancy-free CdS layer, different from TiO_2 with many oxygen vacancies and surface traps activated by light illumination. Moreover, the dense CdS layer was also prepared by the homogeneous precipitation method in a urea

solution by Yang's group.[77] They achieved the highest PCE of 2.27%, which is rather low among the CdS-based PSCs. They mentioned that the low PCEs originated from the inferior perovskite/CdS interface, such as pinholes. We also propose that during this homogeneous precipitation method, the interface of the CdS and FTO might not be compact enough for preventing current leakage.

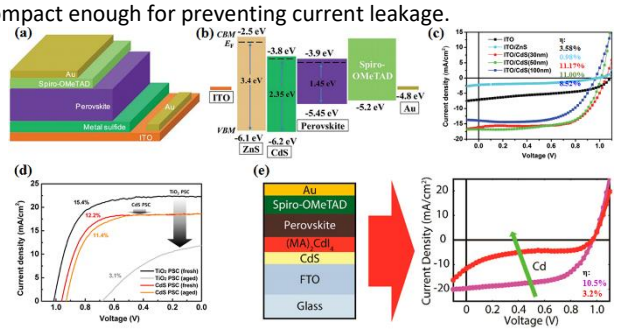

Fig. 6 (a) Device structure, (b) Energy diagram and (c) J-V curves of the PSCs with different device structures.[74] (d) J-V curves comparison of PSCs based on CdS and TiO_2, respectively.[76] (e) Device structure and J-V curve variation of PSCs with Cd doped perovskite layer.[78] Adapted with permission from ref. 74, 76 and 78. Copyright 2015 The Royal Society of Chemistry, 2016 American Chemical Society, 2016 American Chemical Society.

For the CdS-based PSCs, the Cd ions can migrate to the perovskite during the perovskite deposition process or during the working condition of the PSCs. This migration has been studied and found that it has a significant impact on the performance of the PSCs. Mitzi's group did some research on the CdS-based PSCs and a PCE exceeding 15% was achieved.[78] The XPS results revealed the small presence of Cd at the surface of the perovskite film. They deliberately doped Cd into the perovskite film and found that the doping increased the grain size of the perovskite materials, but reduced the PCE (inferred by the S-shape of their J-V curve) by formation of a secondary phase of $(CH_3NH_3)_2CdI_4$, which is an electrical barrier (Fig. 6e). They speculated that the secondary phase should form via the reaction of CdS with MAI during the deposition of the perovskite. Two possible reasons for the reduction in performance with the Cd incorporation were proposed. The first reason is the generation of deep defect states within the band gap of the perovskite. The second one is the introduction of defects at the junctions between the perovskite and CdS layers or at the grain boundaries in the perovskite, or through interfacial reactions involving the formation of secondary phases. Furthermore, they found that excessive annealing lead to a reaction between the CdS and perovskite and degradation of the device performance, while on the other hand, annealing leads to a larger perovskite grain size with reduced carrier recombination at the grain boundary. They determined that 125 °C provided an acceptable compromise between the grain growth and barrier prevention. In 2017, Yu and co-workers also reported the same phenomenon that Cd could be doped into the perovskite film.[79] In their research, a CdS film was prepared via a low temperature (85 °C) chemical bath deposition process and served as an ESL. They prepared the perovskite layer through a two-step physical-chemical evaporation deposition process, which promoted the Cd doping into the perovskite. The doping could engineer the conduction band edge to lower energies. Through this method, the CdS-based PSCs yielded a high PCE of 14.68% for the rigid substrate, while 9.93% for the flexible PET substrate.

As already discussed, CdS might be a potential ESL for PSCs because of its ease of preparation, excellent properties, and proper energy band structure. Additionally, the migration of Cd ions into the perovskite, generating a secondary phase, is an important issue for the CdS-based PSCs.

2.1.6 Other sulfide ESLs

Recently, Tang's group utilized bismuth trisulfide (Bi_2S_3) as the ESL of PSCs for the first time[80]. They pointed out that this compound has several advantages, which make it suitable for electron extraction from the perovskite layer. First, Bi_2S_3 has intrinsically n-type defect properties. According to the first-principles theoretical calculations, Bi_2S_3 possesses intrinsically n-type defects whenever the dominant defects are sulfur vacancies or interstitial sulfur, guaranteeing a high carrier concentration in the Bi_2S_3 film regardless of the preparation process. Secondly, Bi_2S_3 has a high carrier mobility (257 $cm^2V^{-1}s^{-1}$). The third reason is that Bi_2S_3 is composed of one-dimensional $(Bi_4S_6)_n$ ribbons. When processed into an amorphous state, the ordering of these ribbons is ruined, yet the dangling bonds are limited, as in an amorphous chained polymer, thus resulting in a low defect density. In their research, a simple thermal evaporation process was employed to prepare an amorphous Bi_2S_3 film as the ESL of the PSCs with an inverted configuration (Fig. 7a). During the thermal evaporation process, the substrate was kept at room temperature in order to minimize any damage to the as-deposited perovskite layer. With the inverted configuration, the PSCs achieved the highest PCE of 13.1% after optimizing the thickness of the Bi_2S_3 layer (Fig. 7b and c). This decent PCE should be attributed to the high carrier mobility and conductivity of the amorphous Bi_2S_3 and the efficient charge separation at the Bi_2S_3/$MAPbI_3$ interface. Moreover, it was found that the devices possess a very good ambient storage stability due to the hydrophobicity and chemical stability of the Bi_2S_3 ESL.

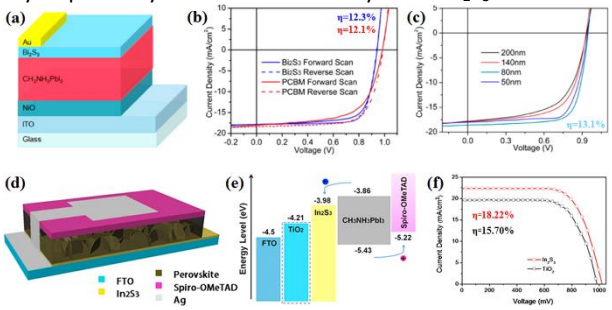

Fig. 7 (a) Schematic demonstration of inverted PSC, (b) J-V curves of devices with Bi_2S_3 and PC61BM as ESL in reverse and forward modes and (c) J-V curves of the PSCs with different Bi_2S_3 film thicknesses.[80] (d) Device architecture, (e) Energy level diagram and (f) J-V curves of the PSCs based on In_2S_3 and TiO_2 ESLs, respectively.[81] Adapted with permission from ref. 80 and 81. Copyright 2016 American Chemical Society, 2017 Elsevier.

Indium trisulfide (In_2S_3) is a highly stable and non-toxic n-type semiconductor with a high carrier mobility (above 17.6 $cm^2V^{-1}s^{-1}$) and moderate band gap (2.0-2.8 eV), all of which are desirable properties for the ESL in PSCs. Very recently, Zhao and co-workers reported In_2S_3 as the ESL of PSCs for the first time.[81] In their research, the In_2S_3 film constructed from well-organized nanoflake arrays was prepared by a low-temperature chemical bath deposition method (Fig. 7d). The device based on In_2S_3 exhibited a higher recombination resistance than that of TiO_2 ESL, meaning better electron extraction ability.

Accompanied with good energy level matching among each component (Fig. 7e) the resultant In_2S_3 based PSCs achieved the high PCE of 18.22% with negligible hysteresis, higher than that of 15.70% for the TiO_2-based PSCs (Fig. 7f). Therefore, they concluded that the optimized band structure, enhanced light trapping of the In_2S_3 ESL and the high carrier separation efficiency are responsible for the high performance.

The research on low-temperature processed metal sulfide ESLs, except for CdS, is still on the initial stage and the literature is limited. Based on the above research, metal sulfides have potentials to replace the traditional TiO_2 ESL in PSCs, not only because of their relatively high performances, but also because of their ease of preparation at low temperature. We are inspired that other low-temperature processed transition metal sulfides should be explored for PSCs with high performance.

2.2 Ternary metal compound ESLs

2.2.1 Zn_2SnO_4 ESLs

Besides the binary metal oxides discussed above, some ternary oxides have also been used as efficient ESLs in recent years. The binary metal oxides easily to be prepared by a simple hydrolysis and oxide process. However, the synthesis of ternary oxides always requires a relatively high energy. For example, the efficient ESLs in PSCs, such as $BaSnO_3$, La-doped $BaSnO_3$ and $BaTiO_3$, are synthesized at high temperature or required high-temperature post sintering.[82-85] In this review, we focus on the low-temperature processed ESLs, thus the high-temperature processed ESLs will be skipped.

Except for the aforementioned ternary oxides, in recent years, Zn_2SnO_4 has been synthesized at low temperature and employed as an efficient ESL. Zn_2SnO_4 has a high-electron Hall mobility of 10-30 $cm^2V^{-1}s^{-1}$, a wide optical band gap of 3.8 eV, a low refractive index of 2.0 in the visible spectrum and a similar conduction band edge position to that of TiO_2. Moreover, Zn_2SnO_4 has a very good chemical stability with respect to acid/base solution and polar organic solvents. Our group synthesized Zn_2SnO_4 nanocrystals and used them in dye-sensitized solar cells, achieving decent PCEs in 2014.[86] Therefore, Zn_2SnO_4 has a good potential of replacing the TiO_2 ESL. Shin and co-workers synthesized highly-dispersed Zn_2SnO_4 nanoparticles at 95 °C, then spin-coated the nanoparticles on a flexible substrate with a post annealing at about 100 °C.[87] The cross-sectional SEM image, photograph and energy levels of the materials are shown in Fig. 8a and b. The Zn_2SnO_4 layer allowed superior transmittance in the visible regions than the bare flexible PEN/ITO substrate due to the antireflection effect of the Zn_2SnO_4. A high PCE of 15.3% was achieved, the highest performance reported at that time for flexible PSCs (Fig. 8c).

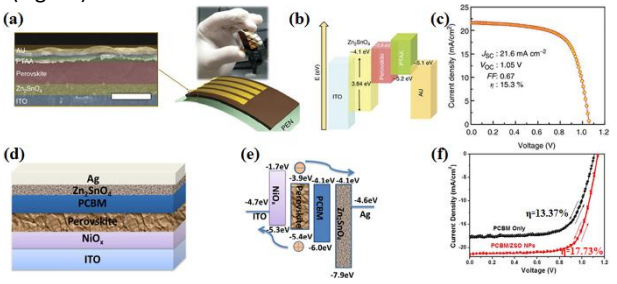

Fig. 8 (a) Cross-sectional SEM image and photograph, (b) Energy levels of the materials and (c) J-V curve of the PSCs based on Zn_2SnO_4 ESL.[87] (d) Device configuration, (e) Energy level diagram and (f) J-V curves of the PSCs based on Zn_2SnO_4 ESL.[88] Adapted with permission from ref. 87 and 88. Copyright 2015 Nature Publishing Group, 2016 The Royal Society of Chemistry.

Soon after these studies, the PCE of the Zn_2SnO_4-based PSCs was further improved by Jen et al. by introducing PCBM into the configuration.[88] Similar to that of Shin et al.'s research, Jen et al. prepared the Zn_2SnO_4 by a hydrothermal process but at the higher reaction temperature of 180 °C. They designed inverted p-i-n PSCs (Fig. 8d and e) in which the PCBM was deposited between the perovskite and Zn_2SnO_4 layer to facilitate the electron transfer from the perovskite to the cathode. As a result, the Zn_2SnO_4-based ESL enabled efficient p-i-n PSCs with the highest PCE of 17.7% (Fig. 8f). At the same time, an initial PCE of over 90% can be retained after a 14-day storage in an ambient environment. This is because that the surface of Zn_2SnO_4-based ESL is more hydrophobic than that of the simple PCBM ESL, as manifested through the contact angle test. For the conventional n-i-p PSCs and flexible PSCs, the PCEs of 14.5% and 11.4% were achieved, respectively. Recently, there are some other studies of the Zn_2SnO_4 ESL for PSCs, such as the Zn_2SnO_4-based composites and mesoporous Zn_2SnO_4.[89-91] But in these reports, the preparation of Zn_2SnO_4 requires a high-temperature annealing at 500 °C or higher, thus they will not be discussed here.

Though the Zn_2SnO_4 is promising as an efficient ESL for PSCs with high PCEs, the preparation process is slightly complex, which might hinder its application for the large-scale production of PSCs.

3 Organic ESLs

3.1 Fullerene ESLs

Fullerenes, such as C60 and PCBM, have been widely used as the ESLs of PSCs because of their high electron transporting abilities. C60 lacks bulky side-chains and can be packed more densely, which facilitates intermolecular charge transport. Furthermore, C60 exhibits the high electron mobility of 1.6 cm^2 $V^{-1}s^{-1}$ and the conductivity of $2.3x10^{-3}$ S cm^{-1}. Recently, C60 thin films have been fabricated by low-temperature processes and employed as ESLs in both inverted and regular structure PSCs.

In 2015, Snaith's group developed efficient PSCs with a regular n-i-p architecture by employing C60 as the ESL, which was prepared by a spin-coating process.[92] Through characterizations, they found that compared to that of the TiO_2 compact layer, the C60 ESL-based devices displayed an enhanced electron extraction from the photo-excited perovskite to the C60 layer. Notably, their luminescent measurements in complete devices showed for the first time by direct observation of the switching on and off charge extraction depending upon the pre-biasing history. In addition, the devices displayed a negligible hysteresis, highly-stabilized PCEs and long-term stability when tested under full sunlight.

In another study, Yan and co-workers demonstrated efficient PSCs using vacuum-processed and room temperature deposited C60 films as the ESL.[93] The best-performing planar PSC using an ultra-thin C60 interface layer achieved a maximum PCE of 15.14% (Fig. 9a, b and c). They demonstrated that the C60 ESL cannot only block hole transport but also passivate the FTO/perovskite interface. Therefore, the PSCs with C60 interface layers showed much higher performances and lower hysteresis than the reference cells without the interface layers. Lee's group recently reported the C60-based

PSCs with similar fabrication processes as that of Yan's work.[94] The optimized C60 ESL with the thickness of 35 nm afforded the best PCE of 19.1%. The C60 layers displayed significant electron transport properties and reduced leakage loss. Furthermore, a hysteresis-free flexible PSC with the PCE of 16.0% was also demonstrated. Thus C60 is really a promising candidate for replacing the traditional high-temperature processed TiO_2 ESL, not only because of the resultant high performances, but also because of its low-temperature processing and compatible with various kinds of substrates.

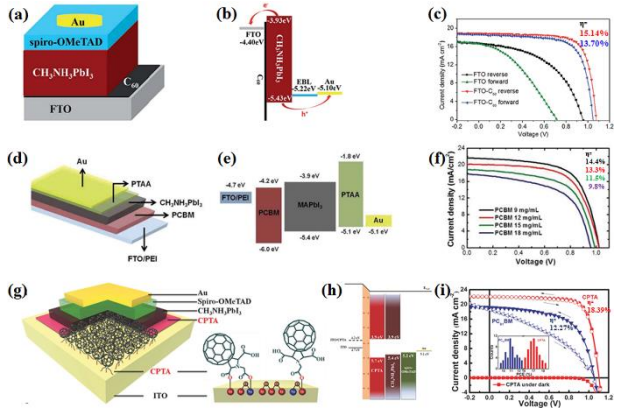

Fig. 9 (a) Device structure, (b) energy band diagram and (c) J-V curves of the PSCs with C60 ESL.[93] (d) Device structure, (e) energy band diagram and (f) J-V curves of the PSCs based on PCBM with different concentrations.[95] (g) Schematic device structure, (h) Corresponding energy level diagram and (i) J-V curves of PSCs based on CPTA (comparison with PC61BM).[96] Adapted with permission from ref. 93, 95 and 96. Copyright 2015 The Royal Society of Chemistry, 2015 The Royal Society of Chemistry, 2017 Wiley.

PCBM is another kind of fullerene that has been widely used as the ESL in PSCs with different configurations. It has been reported that PCBM can efficiently collect and transport electrons through the PCBM/perovskite interface. Moreover, PCBM can effectively passivate grain boundaries and reduce the density of the trap states of the perovskite layer, therefore reducing the hysteresis of the PSCs. To the best of our knowledge, the PCBM ESLs were always fabricated through the low-temperature solution processes.

Yang's group used a single component PCBM as the ESL in inverted structure PSCs in early 2014.[3] The PSCs with a low-temperature solution-processed PCBM achieved the PCE of 11.5% on an ITO substrate, while the flexible PSCs with the PCBM ESL displayed a PCE of 9.2%. Actually, the PCEs of PSCs on the ITO substrate was still lower than that of the conventional high-temperature TiO_2-based PSCs. The main reasons are the imperfect morphology of the perovskite layer induced carrier recombination, Voc and PCE loss. The PCBM then started to be a universal ESL in PSCs, especially in inverted PSCs. At that time, in the most of the studies about the PCBM based PSCs, the inverted p-i-n (conducting substrate/p-type semiconductor layer/perovskite/PCBM/metal electrode) configuration was employed. This is because that if the n-i-p (conducting substrate/PCBM/perovskite/p-type semiconductor layer /metal electrode) architecture was utilized, it would be a challenge to deposit a uniform and dense perovskite layer on the PCBM.

Seok et al. solved this problem of PCBM-based PSCs with the n-i-p configuration.[95] They used a diethylether drip as an orthogonal solvent in the modified solvent engineering process that enabled formation of a dense and uniform perovskite layer without damage to the afore deposited PCBM layer. The configuration of the device and the energy level diagram are shown in Fig. 9d and e. Variation in PCBM concentrations resulted in the PCBM layers with different thicknesses and the optimized device with a 55-nm thick PCBM layer afforded a PCE of 15.3% and a steady-state efficiency of 13.9% (Fig. 9f). Furthermore, the use of the low-temperature processed dense-TiO_2 layer in conjunction with the PCBM layer resulted in an efficiency comparable to that of the single PCBM device, and enabled fabrication of flexible PSCs with the highest PCE of 11.1%. This study provided a new route for fabricating the n-i-p device architecture via a simple and facile solution process. In another similar study, Petrozza et al. reported the TiO_x/PCBM ESL-based PSCs with the n-i-p structure, and the devices reached a relatively high PCE of 17.6% with negligible hysteresis.[97] Numerous pinholes were observed from the perovskite layer deposited on the crystalline TiO_2. While enhanced surface coverage was obtained with the presence of amorphous PCBM. This was induced by the growth of the crystals along different planes, possibly allowing denser packing. The high coverage of the perovskite layer and the efficient charge extraction by the PCBM based ESL were the key criteria for the high efficiency of the PSCs.

In addition, some groups reported the composite PCBM ESLs with organic compounds. For example, Yu and co-workers[98] reported the self-organization method of the [6,6]-phenyl-C61-butyric acid 2-((2-(dimethylamino)-ethyl) (methyl)amino)ethyl ester (PCBDAN) interlayer between the PCBM and ITO for PSCs with the n-i-p structure. The introduction of the self-organized PCBDAN interlayer can effectively reduce the work function of ITO and therefore eliminate the interface barrier between the electron transport layer and electrode. This modification was beneficial for enhancing the charge extraction and decreasing the recombination loss at the interface. With this configuration, they achieved the highest PCE of 18.1% with an almost negligible hysteresis. Furthermore, the PSCs could maintain 85% of its original effciency after 240 h of accelerated UV aging. This is because that PCBM:PCBDAN ESL is stable over long-term operation against UV-light soaking, while the traditional TiO_2 can induce the decomposition of perovskite under UV-light exposure. This self-organization method for the formation of the interlayer is able to not only simplify the fabrication process of low-cost PSCs, but also be compatible with the roll-to-roll processing devices on flexible substrates.

In another study, Kang et al. combined the polyethyleneimine (PEI) surface work function modifier with PCBM, forming the self-assembled organic nanocomposites and acting as the ESL for the PSCs.[99] The low-temperature processed nanocomposite ESL leads to hysteresis-free, planar heterojunction PSCs with stabilized PCEs of over 18%. In addition, the organic nanocomposite was printable and the resultant PSCs displayed a PCE over 17%.

Very recently, another type of fullerene derivative, C60 pyrrolidine tris-acid (CPTA), was attempted to be used as the ESL of the PSCs. Specifically, Fang's group[96] spin-coated the CPTA film on the ITO substrate and fabricated the PSCs with the structure shown in Fig. 10g and energy level shown in Fig. 10h. The best PSC device exhibited a promising PCE of 18.39% and remarkable long-term stability of over 100 days without encapsulation (Fig. 10i). This CPTA

ESL was also applied to flexible PSCs with the excellent PCE of 17.04% and excellent durability against mechanical bending. Moreover, a uniform and robust layer was formed through the esterification of the carboxylic groups of the CPTA molecule with the ITO substrate, noticeably eliminating photocurrent hysteresis effects before and after the bending tests. These results indicated that CPTA is also a promising ESL candidate because of its ease of fabrication and the high PCEs with an excellent stability on both rigid and flexible substrates.

Thus, we concluded that the fullerenes are very efficient ESLs not only due to their high performances and negligible hysteresis, but also ascribed to that they are low-temperature processable. The main disadvantage of the fullerenes ESLs is their high price, which may hinder their applications in the low-cost mass production of the PSCs.

3.2 Non-fullerene Organic ESLs

Beyond the widely used fullerene derivatives, some non-fullerene n-type organic compounds have been utilized as ESLs or a modifier of the ESLs. For example, NunZi's group demonstrated the surface modification of TiO_x by a thin layer of an amorphous 3,4,9,10-perylenetetracarboxylicdiimide-functionalized mexylaminotriazine derivative (PDI-glass) as an interfacial layer.[100] The configuration and the energy levels are shown in Fig. 10a and b. They optimized the thickness of the interfacial PDI-glass layer and the devices showed the best performance with a thickness of 10 nm. The highest PCE of 5.75% was higher than that of 4.11% without the PDI-glass layer (Fig. 10c). We think that the noncompact TiO_x layer and the quality of the perovskite layer are the main reasons for the low performances of the PSCs. The PDI-glass has the effect of promoting the electron extraction in the PSCs.

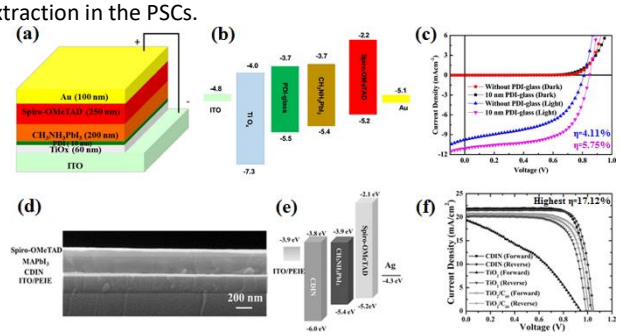

Fig. 10 (a) Device structure, (b) energy band diagram and (c) J-V curves of the PSCs with PDI ESL.[100] (d) Cross-sectional SEM image, (e) Energy levels diagram and (f) J-V curves of PSCs based on CDIN ESL.[101] Adapted with permission from ref. 100 and 101. Copyright 2017 Elsevier, 2016 Wiley.

In another study, Jen and co-workers developed a low-temperature, solution-processable organic ESL comprised of a discotic coronene diimide (CDI) core with an expanded π-conjugated plane along the short axis of the perylene diimide (PDI), enabling a more efficient face-on π-π stacking in the solid-state to provide a good charge carrier mobility.[101] Furthermore, the CDI core was functionalized with polar 3-(dimethylamino)propyl moieties, such as N,N¢'-bis(3-(dimethylamino)propyl)-5,11-dioctylcoronene-2,3,8,9-tetracarboxdiimide (CDIN) to modulate the polarity of the ESL for enhancing the crystal growth of the atop perovskites. As a result, the derived n-i-p PSC on the rigid ITO showed the high PCE of 17.1% (Fig. 10d, e and f), outperforming that of the device using a regular TiO_2 ESL. Benefitting from the low-temperature solution processability of CDIN, a flexible PSC also achieved the high PCE of 14.2%.

Thus, we can conclude that some non-fullerenes have significant potentials to act as efficient electron transport layers in the PSCs. In future studies, low-temperature processable and cheap non-fullerenes are waiting to be explored, which will be compatible with the printing process for both rigid and flexible devices.

4 QDs ESLs

4.1 CdSe QDs ESLs

QDs have been widely used in photovoltaics due to their remarkable properties, including a tunable band gap, inherently high absorption coefficient, hot electron transfer and multiple exciton generations.[102] CdSe is an n-type semiconductor with a good chemical stability and has a superior hydrophobicity. More importantly, CdSe has a much higher electron mobility (450-900 $cm^2V^{-1}s^{-1}$) than that of TiO_2.[103, 104]

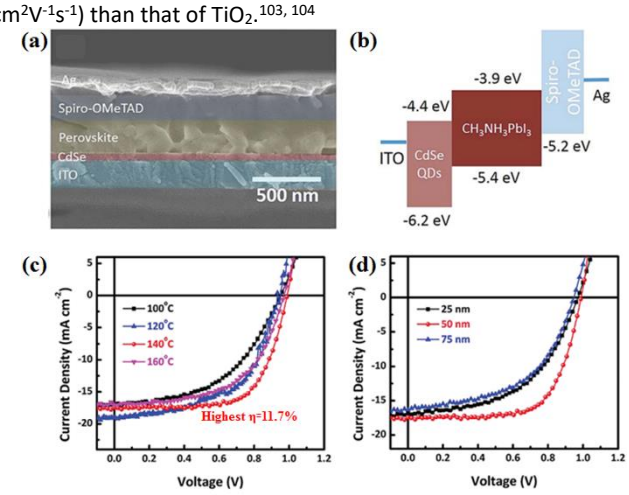

Fig. 11 (a) Cross-sectional SEM image, (b) Energy levels of the CdSe QDs based PSCs; (c) and (d) J-V curves of PSCs based on CdSe QDs obtained under different temperatures and with different thickness.[103] Adapted with permission from ref. 103. Copyright 2014 The Royal Society of Chemistry.

As early as 2014, Li and co-worker tried to use CdSe QDs in a PSC as an ESL.[103] The configuration and energy levels are shown in Fig. 11a and b, respectively. The CdSe DQs were prepared by a hot-injection method followed by a ligand exchange with pyridine. The pyridine replaced the long chain surfactant on CdSe and thus enhanced the electron mobility of the CdSe film. The relatively high PCE at that time of 11.7% was achieved, which indicated that the CdSe nanocrystals are an efficient ESL material for PSCs (Fig. 11c). They concluded that 140 °C is the proper temperature and 50 nm is the most suitable film thickness (Fig. 11c and d). More recently, Zang et al. utilized a CdSe quantum dot/PCBM composite as an ESL and investigated the structure, stability and performance of the PSCs.[104] They found that CdSe/PCBM could reduce the roughness of the perovskite, leading to a high-quality perovskite layer. Their density functional theory calculations showed that there was a strong atomic orbital hybridization between CdSe and perovskite, much stronger than that between CdSe and CH_3NH_3, thus the perovskite layer possesses an excellent chemical stability. Moreover, the superior hydrophobicity of CdSe inhibits water penetration into the

perovskite layer, which substantially improves the stability of the device. PSCs using the CdSe/PCBM composite as the ESL exhibited the highest PCE of 13.7% after optimizing the CdSe content in the composites. The high PCEs were attributed to the CdSe doping, which induced an in-built electric field between the perovskite and CdSe, leading to an efficient electron-hole separation. These results indicated that the CdSe is playing multiple roles in enhancing the PCE and improving the stability of the devices. Even though the studies of QDs ESL are limited, employing QDs as an ESL is meaningful because it can provide us a new aspect for ESL research.

5 Summary

In this review, we introduced the very recent developments in low-temperature processed non-TiO_2 ESLs including inorganic, organic and QDs ESLs. We summarized the preparation methods for the above ESLs, as shown in Fig. 12. We can find that the spin-coating process is the most prevalent method, resulting from its ease of operation, low cost and high quality of the resultant film. Moreover, we summarized the low-temperature processed non-TiO_2 ESLs and the performances of the resultant PSCs in Tab. 1 and Fig. 13.

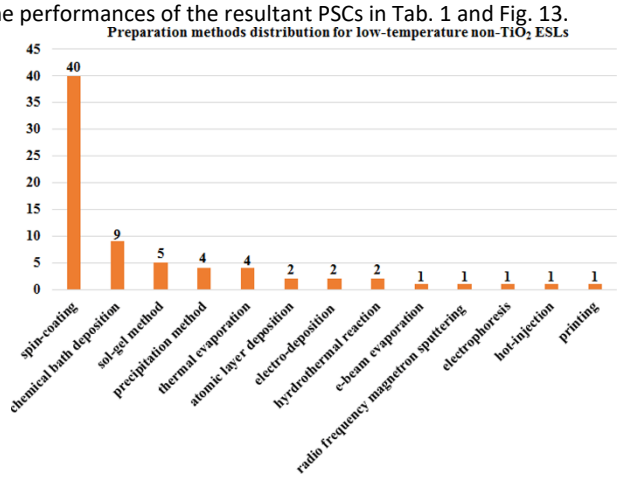

Fig. 12 Preparation methods distribution for low-temperature processed non-TiO_2 ESLs.

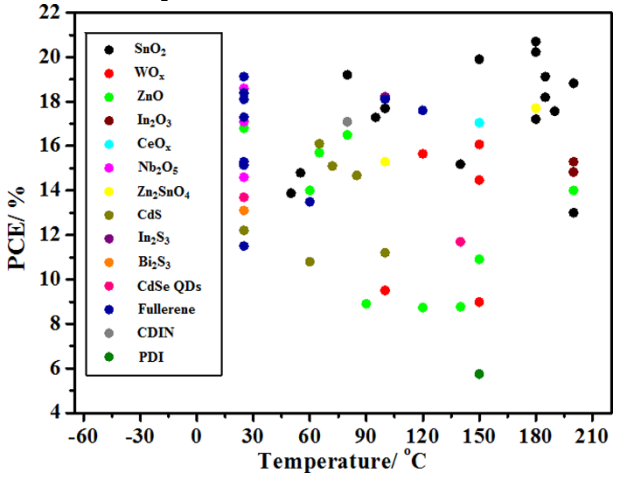

Fig. 13 PCE distributions of PSCs based on various low-temperature processed non-TiO_2 ESLs obtained at different temperatures.

		ESL	preparation method	preparation temperature(℃)	perovskite layer	Champion PCE(%) on rigid susbtrate	Champion PCE(%) of Flexible PSC	Ref.
Inorganic ESLs	SnO_2	SnO_2	sol-gel & spin-coating	80	$(FAPbI_3)_{0.85}(MAPbBr_3)_{0.15}$	19.2	16.11	32
		SnO_2	spin-coating	180	$MAPbI_3$	17.21	N/A	33
		SnO_2	spin-coating & chemical bath deposition	180	$Cs_xFA_yMA_{1-x-y}Pb(I_zBr_{1-z})_3$	20.7	N/A	34
		a-SnO_2	chemical bath deposition	55	$MAPbI_3$	14.8	N/A	35
		SnO_2	electro-deposition technique	50	$MAPbI_3$	13.88	N/A	37
		SnO_2	plasma-enhanced atomic layer deposition	100	$MA_{0.7}FA_{0.3}PbI_3$	N/A	18.36	38
		Li-doped SnO_2	spin-coating	185	$MAPbI_3$	18.2	14.78	39
		SnO_2	spin-coating	200	$MAPbI_3$	13	N/A	40
		SnO_2	spin-coating	150	$(FAPbI_3)_{0.97}(MAPbBr_3)_{0.03}$	19.9	N/A	41
		Sb-doped SnO_2	oil bath & spin-coating	100	$MAPbI_3$	17.7	N/A	42
		SnO_2/graphene quantum dots	spin-coating	180	$MAPbI_3$	20.23	N/A	43
		Y-Doped SnO_2	hyrdrothermal reaction	95	$MAPbI_3$	17.29	N/A	44
		Nb-doped SnO_2	spin-coating	190	$(FAPbI_3)_{0.85}(MAPbBr_3)_{0.15}$	17.57	N/A	45
		MgO/SnO_2	spin-coating	200	$MAPbI_3$	18.82	N/A	46
		SnO_2/PCBM	spin-coating	185	$MAPbI_3$	19.12	N/A	47
		SnO_2/C60	spin-coating	140	$MAPbI_3$	15.18	N/A	48
	ZnO	ZnO	chemical bath deposition	90	$MAPbI_3$	8.9	2.62	49
		ZnO	electro-deposition technique	150	$MAPbI_3$	10.91	N/A	50
		ZnO	sol-gel & spin-coating	140	$MAPbI_3$	8.77	N/A	51
		ZnO	atomic layer deposition	80	$MAPbI_3$	16.5	N/A	52
		ZnO	precipitation method & spin-coating	65	$MAPbI_3$	15.7	10.2	53
		ZnO	precipitation method & spin-coating	60	$MAPbI_3$	14	N/A	55
		ZnO	precipitation method & spin-coating	120	$MAPbI_3$	8.73	4.29	56
		ZnO/SnO_2	spin-coating	200	$MAPbI_3$	14	N/A	57
		ZnO/PCBM	spin-coating	RT	$MAPbI_xCl_{3-x}$	16.8	N/A	59
	WO_x	WO_x-TiO_x	spin-coating	150	$MAPbI_3$	14.47	N/A	61
		WO_x	spin-coating	150	$MAPbI_xCl_{3-x}$	8.99	N/A	62
		W(Nb)O_x	spin-coating	120	$MAPbI_xCl_{3-x}$	N/A	15.65	63
		WO_x/C60	spin-coating	150	$MAPbI_3$	16.07	N/A	64
		WO_3	spin-coating	100	$MAPbI_xCl_{3-x}$	9.5	N/A	65
	Other oxides	CeO_x	sol-gel & spin-coating	150	$MAPbI_3$	17.04	N/A	66
		Nb_2O_5	e-beam evaporation	RT	$MA_{0.33}FA_{0.66}Pb(Br_{0.16}I_{0.84})_3$	18.59	15.56	68
		a-Nb_2O_5	radio frequency magnetron sputtering	RT	$MAPbI_3$	17.1	12.1	69
		Nb_2O_5	electrophoresis	RT	$MAPbI_3$	14.6	N/A	70
		In_2O_3/PCBM	sol-gel & spin-coating	200	$MAPbI_3$	14.83	N/A	72
	CdS	CdS	chemical bath deposition	60	$MAPbI_3$	10.8	N/A	73
		CdS	spin-coating	100	$MAPbI_3$	11.2	N/A	74
		CdS	chemical bath deposition	65	$MAPbI_3$	16.1	N/A	75
		CdS	thermal evaporation	RT	$MAPbI_3$	12.2	N/A	76
		CdS	homogeneous precipitation	90	$MAPbI_3$	2.27	N/A	77
		CdS	chemical bath deposition	72	$MAPbI_3$	15.1	N/A	78
		CdS	chemical bath deposition	85	$MAPbI_3$	14.68	9.9	79
	Bi_2S_3	Bi_2S_3	thermal evaporation	RT	$MAPbI_3$	13.1	N/A	80
	In_2S_3	In_2S_3	chemical bath deposition	100	$MAPbI_3$	18.22	N/A	81
	Zn_2SnO_4	Zn_2SnO_4	spin-coating	100	$MAPbI_3$	N/A	15.3	87
		Zn_2SnO_4	hyrdrothermal & spin-coating	180	$MA_xFA_{1-x}Pb(I_yBr_{1-y})_3$	17.7	11.4	88
		a: amorphous		RT: room temperature	MA: methylammonium FA: formamidinium			

Tab. 1 Preparation methods of inorganic ESLs and performances of resultant PSCs

As for the inorganic ESLs, low-temperature processed binary metal oxides are the ideal alternatives of TiO_2, not only because of their promising high performance, but also for their low cost and

easy preparation. As we can see in Fig. 13 and Tab. 1, among the various inorganic ESLs, SnO_2 is the most promising material as the SnO_2-based PSCs always display high PCEs, because the conductivity and the surface coverage of the film on the substrate are highly dependent on the annealing temperature. Therefore, seeking a balance between a low-temperature preparation and the uniform morphology is a very important topic for the binary oxide film. We think that metal doping and second phase compositing, with the effects of tuning the conduction band position and enhancing the electron transferring efficiency, are reliable ways to further improve the performances of binary oxide ESL-based PSCs. Binary metal sulfides are also used in PSCs as ESLs and decent PCEs were achieved, although not as high as PSCs with metal oxide ESLs. However, the impacts of sulfides on the perovskite layer, such as the generation of a secondary phase acting as an electrical barrier, still lack sufficient studies. Several kinds of ternary metal compounds have been used as ESLs, while the low-temperature processable compound is currently only Zn_2SnO_4. The hydrothermal process and spin-coating method were utilized to prepare Zn_2SnO_4 films and high performances were achieved. We think that other new materials with a low-temperature processability need to be developed.

		ESL	preparation method	preparation temperature (°C)	perovskite layer	Champion PCE(%) on rigid susbtrate	Champion PCE(%) of Flexible PSC	Ref.
Organic ESLs	Fullerene	C60	spin-coating	60	$MAPbI_xCl_{3-x}$	13.5	N/A	92
		C60	thermal evaporation	RT	$MAPbI_3$	15.14	N/A	93
		C60	thermal evaporation	RT	$MAPbI_3$	19.12	16	94
		C60 pyrrolidine tris-acid	spin-coating	RT	$MAPbI_3$	18.39	17.04	96
		PCBM	spin-coating	RT	$MAPbI_xCl_{3-x}$	11.5	9.2	3
		PCBM	spin-coating	RT	$MAPbI_3$	15.3	11.1	95
		TiOx/PCBM	spin-coating	120	$MAPbI_3$	17.6	N/A	97
		PCBM:PCBDAN	spin-coating	100	$MAPbI_3$	18.1	14.2	98
		PCBM:PEI	printing	RT	$MAPbI_3$	17.3	N/A	99
	Non-fullerene	TiOx/PDI-glass	chemical bath deposition &	150	$MAPbI_3$	5.75	N/A	100
		CDIN	spin-coating	80	$MAPbI_3$	17.1	14.2	101
				RT: room temperature	MA: methylammo			

Tab. 2 Preparation methods of organic ESLs and performances of resultant PSCs

As shown in Fig. 13 and Tab. 2, organic ESLs, such as fullerene derivatives and non-fullerenes, have been widely used in PSCs and very high PCEs were achieved. Because they are low-temperature processable, versatile in various configurations and with promising high performances, organic materials, especially fullerene derivatives are very suitable ESLs. As we can see in Fig. 13, the PCEs of most fullerene-based PSCs have high PCE values. However, there is an important issue that the price of these organic materials is much higher than the traditional TiO_2. Therefore, in the future, while maintaining high performances, the price of them should be reduced or new types organic materials with low prices should be explored.

		ESL	preparation method	preparation temperature (°C)	perovskite layer	Champion PCE(%) on rigid susbtrate	Champion PCE(%) of Flexible PSC	Ref.
QDs ESLs	CdSe QDs	CdSe QDs	hot-injection	140	$MAPbI_3$	11.7	N/A	103
		CdSe QDs/PCBM	spin-coating	RT	$MAPbI_xCl_{3-x}$	13.7	N/A	104
				RT: room temperature	MA: methylammonium			

Tab. 3 Preparation methods of QDs ESLs and performances of resultant PSCs

QDs were reported as ESLs and researchers proved that the chemical stability of the perovskite can be enhanced by the strong orbital hybridization effect of the perovskite and QDs. However, the efficiencies of QDs ESL-based PSCs, compared to PSCs with other kinds of ESLs are still very low, thus they need to be further improved as shown in Fig. 13 and Tab. 3.

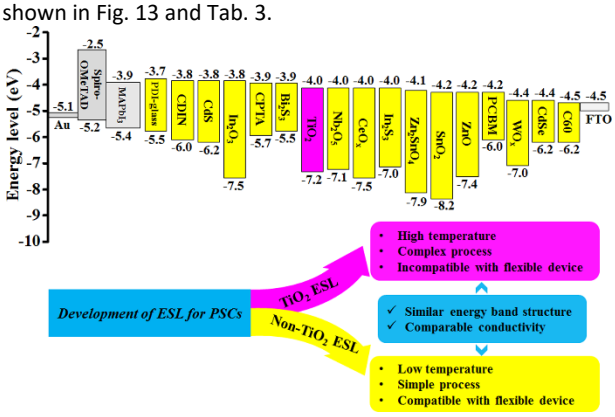

Fig. 14 Schematic of energy level distributions for different ESLs of PSCs and comparison of TiO_2 and non-TiO_2 ESLs

Fig. 14 shows the energy level distributions of different ESLs from the literatures. It shows that non-TiO_2 ESLs possess similar energy band structure with that of TiO_2, which enable efficient electron extraction from the perovskite. Moreover, these non-TiO_2 ESLs possess comparable conductivity over the TiO_2, thus the electrons from the perovskite can be rapidly transformed to the FTO electrode with suppressed charge recombination process. The advantages of non-TiO_2 ESLs over the traditional TiO_2 ESL are low-temperature processable and energy-efficient. Specifically, the non-TiO_2 ESLs require only low temperature and short operating duration for post-treatment, which will simplify the processes of PSC fabrication. Another significant advantage is that the non-TiO_2 ESLs are compatible with the flexible devices, credited to its low preparation temperature which is withstandable for the flexible substrate. The low-temperature processable non-TiO_2 ESLs are envisioned to be able to promote the industrial printing processes and reduce the production costs of wearable electronics.

In summary, the low-temperature fabrication of ESLs can ensure the low cost and simply fabrication processes of PSCs, maintain performances comparable to those of the high-temperature processed TiO_2-based PSCs, and be compatible with flexible devices. Thus it is a very meaningful to replace traditional high-temperature TiO_2 ESLs with low-temperature processed non-TiO_2 ESLs.

6 Outlook

As summarized in this review, the low-temperature processed ESLs have recently achieved much progress in both the material varieties and performance. However, the performances of some ESLs are still not comparable to that of the basic TiO_2 PSCs at high-temperature, thus several issues as follows need to be addressed.

First, an ideal non-TiO_2 ESL should be further reduced in cost, appropriate to fast and large area preparation. Low cost includes two aspects, the inexpensive material and low preparation costs. Many kinds of non-TiO_2 ESLs, such as fullerenes and rare metal oxides, are much more expensive than that of TiO_2. Until now, there are still some non-TiO_2 ESL materials synthesized at temperatures over 100 °C, such as SnO_2, In_2O_3 and Zn_2SnO_4. This temperature also causes wasted energy and equipment costs, which will hinder their practical

application in the commercialized PSCs, even though non-TiO_2 ESLs can provide high performances.

Second, proper ESLs must have a significant electron transferring ability. The electron-transport layer also serves as the hole-blocking layer to mitigate recombination at the interface. To possess an excellent PCE performance, ESLs should have their energy band alignment optimized to that of the perovskite layer, which will result in a lower Voc loss or insufficient electron transport from the perovskite to the ESLs. This alignment includes element doping, surface passivation, compositing a second phase, and heteroepitaxial growth, which can increase the electron extraction efficiency and block hole transferring.

Third, the correlation between the conductivity, the surface coverage and the preparation temperature of the ESL is an important issue. Usually, a low annealing temperature leads to an unsatisfactory conductivity and surface coverage, which results in more electron-hole recombination between the heterogeneous interface of the perovskite and ESLs. Increasing the temperature will raise the cost and hinder the realization of an all-low-temperature fabrication of the PSCs. Moreover, as shown in Table 1, not all low-temperature processed ESLs were used in flexible devices because the preparation temperature of the ESLs is still high. Therefore, a balance between lowering the preparation temperature and maintaining the high performance of the PSCs should be paid attention to in future studies. In spite of this, the low-temperature processed ESLs are also great alternatives of the traditional TiO_2 ESL, and in the future, more kinds of low-temperature processable ESLs will be explored to reduce the cost and simplify the fabrication process of efficient PSCs.

7 Conflicts of interest

There are no conflicts to declare.

8 Acknowledgements

This work was supported by the Grant-in-Aid for Scientific Research (KAKENHI) program, Japan (C, Grant Number 15K05597) and Takahashi Industrial and Economic Research Foundation (Takahashi Grant Number 06-003-154). The authors would like to thank the Research Center for Solar Light Energy Conversion, Kyushu Institute of Technology for their support.

9 Reference

1. A. Kojima, K. Teshima, Y. Shirai and T. Miyasaka, *J. Am. Chem. Soc.*, 2009, **131**, 6050-6051.
2. https://www.nrel.gov/pv/assets/images/efficiency-chart.png.
3. J. You, Z. Hong, Y. M. Yang, Q. Chen, M. Cai, T.-B. Song, C.-C. Chen, S. Lu, Y. Liu and H. Zhou, *ACS Nano*, 2014, **8**, 1674-1680.
4. N. J. Jeon, J. H. Noh, Y. C. Kim, W. S. Yang, S. Ryu and S. I. Seok, *Nat. Mater.*, 2014, **13**, 897-903.
5. H. S. Jung and N. G. Park, *Small*, 2015, **11**, 10-25.
6. M. A. Green, A. Ho-Baillie and H. J. Snaith, *Nat. Photonics*, 2014, **8**, 506-514.
7. J. Seo, J. H. Noh and S. I. Seok, *Acc. Chem. Res.*, 2016, **49**, 562-572.
8. Z. Yu and L. Sun, *Adv. Energy Mater.*, 2015, **5**, 1500213.
9. M. M. Lee, J. Teuscher, T. Miyasaka, T. N. Murakami and H. J. Snaith, *Science*, 2012, **338**, 643-647.
10. T. Tyson, W. Gao, Y.-S. Chen, S. Ghose and Y. Yan, *Sci. Rep.*, 2017, **7**, 9401.
11. Y. Yang, M. Yang, D. T. Moore, Y. Yan, E. M. Miller, K. Zhu and M. C. Beard, *Nature Energy*, 2017, **2**, 16207.
12. W. Chen, Y. Wu, Y. Yue, J. Liu, W. Zhang, X. Yang, H. Chen, E. Bi, I. Ashraful and M. Grätzel, *Science*, 2015, **350**, 944-948.
13. T. Leijtens, G. E. Eperon, S. Pathak, A. Abate, M. M. Lee and H. J. Snaith, *Nat. Commun.*, 2013, **4**, 2885.
14. Y. Guo, C. Liu, H. Tanaka and E. Nakamura, *J. Phys. Chem. Lett.*, 2015, **6**, 535-539.
15. C. S. Ponseca Jr, T. J. Savenije, M. Abdellah, K. Zheng, A. Yartsev, T. r. Pascher, T. Harlang, P. Chabera, T. Pullerits and A. Stepanov, *J. Am. Chem. Soc.*, 2014, **136**, 5189-5192.
16. X. Deng, G. C. Wilkes, A. Z. Chen, N. S. Prasad, M. C. Gupta and J. J. Choi, *J. Phys. Chem. Lett.*, 2017, **8**, 3206-3210.
17. J. T.-W. Wang, J. M. Ball, E. M. Barea, A. Abate, J. A. Alexander-Webber, J. Huang, M. Saliba, I. Mora-Sero, J. Bisquert and H. J. Snaith, *Nano Lett.*, 2013, **14**, 724-730.
18. H. Li, W. Shi, W. Huang, E.-P. Yao, J. Han, Z. Chen, S. Liu, Y. Shen, M. Wang and Y. Yang, *Nano Lett.*, 2017, **17**, 2328-2335.
19. U. K. Thakur, A. M. Askar, R. Kisslinger, B. D. Wiltshire, P. Kar and K. Shankar, *Nanotechnology*, 2017, **28**, 274001.
20. G. Yin, J. Ma, H. Jiang, J. Li, D. Yang, F. Gao, J. Zeng, Z. Liu and S. F. Liu, *ACS Appl. Mater. Interfaces*, 2017, **9**, 10752-10758.
21. Q. Cui, X. Zhao, H. Lin, L. Yang, H. Chen, Y. Zhang and X. Li, *Nanoscale*, 2017, **9**, 18897-18907.
22. R. Ranjan, A. Prakash, A. Singh, A. Singh, A. Garg and R. K. Gupta, *J. Mater. Chem. A*, 2017, 10.1039/C1037TA09193A.
23. D. Yang, R. Yang, J. Zhang, Z. Yang, S. F. Liu and C. Li, *Energy Environ. Sci.*, 2015, **8**, 3208-3214.
24. B. J. Kim, D. H. Kim, Y.-Y. Lee, H.-W. Shin, G. S. Han, J. S. Hong, K. Mahmood, T. K. Ahn, Y.-C. Joo and K. S. Hong, *Energy Environ. Sci.*, 2015, **8**, 916-921.
25. Y.-F. Chiang, J.-Y. Jeng, M.-H. Lee, S.-R. Peng, P. Chen, T.-F. Guo, T.-C. Wen, Y.-J. Hsu and C.-M. Hsu, *Phys. Chem. Phys. Chem.*, 2014, **16**, 6033-6040.
26. P. Docampo, J. M. Ball, M. Darwich, G. E. Eperon and H. J. Snaith, *Nat. Commn.*, 2013, **4**, 2761.
27. G. Yang, H. Tao, P. Qin, W. Ke and G. Fang, *J. Mater. Chem. A*, 2016, **4**, 3970-3990.
28. W.-Q. Wu, D. Chen, R. A. Caruso and Y.-B. Cheng, *J. Mater. Chem. A*, 2017, **5**, 10092-10109.

29. M. A. Haque, A. D. Sheikh, X. Guan and T. Wu, *Adv. Energy Mater.*, 2017, **7**, 1602803.
30. Q. Dong, Y. Shi, K. Wang, Y. Li, S. Wang, H. Zhang, Y. Xing, Y. Du, X. Bai and T. Ma, *J. Phys. Chem. C*, 2015, **119**, 10212-10217.
31. Q. Dong, M. Wang, Q. Zhang, F. Chen, S. Zhang, J. Bian, T. Ma, L. Wang and Y. Shi, *Nano Energy*, 2017, **38**, 358-367.
32. Q. Dong, Y. Shi, C. Zhang, Y. Wu and L. Wang, *Nano Energy*, 2017, **40**, 336-344.
33. W. Ke, G. Fang, Q. Liu, L. Xiong, P. Qin, H. Tao, J. Wang, H. Lei, B. Li and J. Wan, *J. Am. Chem. Soc.*, 2015, **137**, 6730-6733.
34. E. H. Anaraki, A. Kermanpur, L. Steier, K. Domanski, T. Matsui, W. Tress, M. Saliba, A. Abate, M. Grätzel and A. Hagfeldt, *Energy Environ. Sci.*, 2016, **9**, 3128-3134.
35. J. Barbé, M. L. Tietze, M. Neophytou, B. Murali, E. Alarousu, A. E. Labban, M. Abulikemu, W. Yue, O. F. Mohammed and I. McCulloch, *ACS Appl. Mater. Interfaces*, 2017, **9**, 11828-11836.
36. X. Liu, K. W. Tsai, Z. Zhu, Y. Sun, C. C. Chueh and A. K. Y. Jen, *Adv. Mater. Interfaces*, 2016, **3**, 1600122.
37. J.-Y. Chen, C.-C. Chueh, Z. Zhu, W.-C. Chen and A. K.-Y. Jen, *Sol. Energy Mater. Sol. Cells*, 2017, **164**, 47-55.
38. C. Wang, L. Guan, D. Zhao, Y. Yu, C. R. Grice, Z. Song, R. A. Awni, J. Chen, J. Wang and X. Zhao, *ACS Energy Lett.*, 2017, **2**, 2118-2124.
39. M. Park, J.-Y. Kim, H. J. Son, C.-H. Lee, S. S. Jang and M. J. Ko, *Nano Energy*, 2016, **26**, 208-215.
40. J. Song, E. Zheng, J. Bian, X.-F. Wang, W. Tian, Y. Sanehira and T. Miyasaka, *J. Mater. Chem. A*, 2015, **3**, 10837-10844.
41. Q. Jiang, L. Zhang, H. Wang, X. Yang, J. Meng, H. Liu, Z. Yin, J. Wu, X. Zhang and J. You, *Nat. Energy*, 2016, **2**, 16177.
42. Y. Bai, Y. Fang, Y. Deng, Q. Wang, J. Zhao, X. Zheng, Y. Zhang and J. Huang, *ChemSusChem*, 2016, **9**, 2686-2691.
43. J. Xie, K. Huang, X. Yu, Z. Yang, K. Xiao, Y. Qiang, X. Zhu, L. Xu, P. Wang and C. Cui, *ACS Nano*, 2017, **11**, 9176–9182.
44. G. Yang, H. Lei, H. Tao, X. Zheng, J. Ma, Q. Liu, W. Ke, Z. Chen, L. Xiong and P. Qin, *Small*, 2017, **13**, 1601769.
45. X. Ren, D. Yang, Z. Yang, J. Feng, X. Zhu, J. Niu, Y. Liu, W. Zhao and S. F. Liu, *ACS Appl. Mater. Interfaces*, 2017, **9**, 2421-2429.
46. J. Ma, G. Yang, M. Qin, X. Zheng, H. Lei, C. Chen, Z. Chen, Y. Guo, H. Han and X. Zhao, *Adv. Sci.*, 2017, **4**, 1700031.
47. W. Ke, D. Zhao, C. Xiao, C. Wang, A. J. Cimaroli, C. R. Grice, M. Yang, Z. Li, C.-S. Jiang and M. Al-Jassim, *J. Mater. Chem. A*, 2016, **4**, 14276-14283.
48. C. Wang, C. Xiao, Y. Yu, D. Zhao, R. A. Awni, C. R. Grice, K. Ghimire, D. Constantinou, W. Liao and A. J. Cimaroli, *Adv. Energy Mater.*, 2017, **7**, 1700414.
49. M. H. Kumar, N. Yantara, S. Dharani, M. Graetzel, S. Mhaisalkar, P. P. Boix and N. Mathews, *Chem. Commun.*, 2013, **49**, 11089-11091.
50. J. Zhang, E. J. Juárez-Pérez, I. Mora-Seró, B. Viana and T. Pauporté, *J. Mater. Chem. A*, 2015, **3**, 4909-4915.
51. M. A. Mahmud, N. K. Elumalai, M. B. Upama, D. Wang, K. H. Chan, M. Wright, C. Xu, F. Haque and A. Uddin, *Sol. Energy Mater. Sol. Cells*, 2017, **159**, 251-264.
52. C.-Y. Chang, K.-T. Lee, W.-K. Huang, H.-Y. Siao and Y.-C. Chang, *Chem. Mater.*, 2015, **27**, 5122-5130.
53. D. Liu and T. L. Kelly, *Nat. Photon.*, 2014, **8**, 133-138.
54. C. M. O. Pelicano and H. Yanagi, *J. Mater. Chem. C*, 2017, **5**, 8059-8070.
55. G. S. Han, H. W. Shim, S. Lee, M. L. Duff and J. K. Lee, *ChemSusChem*, 2017, **10**, 2425-2430.
56. H. Zhou, Y. Shi, K. Wang, Q. Dong, X. Bai, Y. Xing, Y. Du and T. Ma, *J. Phys. Chem. C*, 2015, **119**, 4600-4605.
57. J. Song, E. Zheng, X.-F. Wang, W. Tian and T. Miyasaka, *Sol. Energy Mater. Sol. Cells*, 2016, **144**, 623-630.
58. X. Jia, L. Zhang, Q. Luo, H. Lu, X. Li, Z. Xie, Y. Yang, Y.-Q. Li, X. Liu and C.-Q. Ma, *ACS Appl. Mater. Interfaces*, 2016, **8**, 18410-18417.
59. L. Q. Zhang, X. W. Zhang, Z. G. Yin, Q. Jiang, X. Liu, J. H. Meng, Y. J. Zhao and H. L. Wang, *J. Mater. Chem. A*, 2015, **3**, 12133-12138.
60. K. Mahmood, B. S. Swain, A. R. Kirmani and A. Amassian, *J. Mater. Chem. A*, 2015, **3**, 9051-9057.
61. K. Wang, Y. Shi, Q. Dong, Y. Li, S. Wang, X. Yu, M. Wu and T. Ma, *J. Phys. Chem. Lett.*, 2015, **6**, 755-759.
62. K. Wang, Y. Shi, B. Li, L. Zhao, W. Wang, X. Wang, X. Bai, S. Wang, C. Hao and T. Ma, *Adv. Mater.*, 2016, **28**, 1891-1897.
63. K. Wang, Y. Shi, L. Gao, R. Chi, K. Shi, B. Guo, L. Zhao and T. Ma, *Nano Energy*, 2017, **31**, 424-431.
64. V. O. Eze, Y. Seike and T. Mori, *Org. Electron.*, 2017, **46**, 253-262.
65. A. Gheno, T. T. T. Pham, C. Di Bin, J. Bouclé, B. Ratier and S. Vedraine, *Sol. Energy Mater. Sol. Cells*, 2017, **161**, 347-354.
66. X. Wang, L.-L. Deng, L.-Y. Wang, S.-M. Dai, Z. Xing, X.-X. Zhan, X.-Z. Lu, S.-Y. Xie, R.-B. Huang and L.-S. Zheng, *J. Mater. Chem. A*, 2017, **5**, 1706-1712.
67. A. Kogo, Y. Numata, M. Ikegami and T. Miyasaka, *Chem. Lett.*, 2015, **44**, 829-830.
68. J. Feng, Z. Yang, D. Yang, X. Ren, X. Zhu, Z. Jin, W. Zi, Q. Wei and S. F. Liu, *Nano Energy*, 2017, **36**, 1-8.
69. X. Ling, J. Yuan, D. Liu, Y. Wang, Y. Zhang, S. Chen, H. Wu, F. Jin, F. Wu and G. Shi, *ACS Appl. Mater. Interfaces*, 2017, **9**, 23181-23188.
70. Y.-T. Huang, R. Cheng, P. Zhai, H. Lee, Y.-H. Chang and S.-P. Feng, *Electro. Acta*, 2017, **236**, 131-139.
71. P. Chen, X. Yin, M. Que, X. Liu and W. Que, *J. Mater. Chem. A*, 2017, **5**, 9641-9648.
72. M. Qin, J. Ma, W. Ke, P. Qin, H. Lei, H. Tao, X. Zheng, L. Xiong, Q. Liu and Z. Chen, *ACS Appl. Mater. Interfaces*, 2016, **8**, 8460-8466.
73. M. Abulikemu, J. Barbé, A. El Labban, J. Eid and S. Del Gobbo, *Thin Solid Films*, 2017, **636**, 512-518.

74. J. Liu, C. Gao, L. Luo, Q. Ye, X. He, L. Ouyang, X. Guo, D. Zhuang, C. Liao and J. Mei, *J. Mater. Chem. A*, 2015, **3**, 11750-11755.
75. H. Peng, W. Sun, Y. Li, W. Yan, P. Yu, H. Zhou, Z. Bian and C. Huang, *J. Photonics Energy*, 2016, **6**, 022002.
76. I. Hwang and K. Yong, *ACS Appl. Mater. Interfaces*, 2016, **8**, 4226-4232.
77. J. Wang, L. Liu, S. Liu, L. Yang, B. Zhang, S. Feng, J. Yang, X. Meng, W. Fu and H. Yang, *Sust. Energy Fuels*, 2017, **1**, 504-509.
78. W. A. Dunlap-Shohl, R. Younts, B. Gautam, K. Gundogdu and D. B. Mitzi, *J. Phys. Chem. C*, 2016, **120**, 16437-16445.
79. G. Tong, Z. Song, C. Li, Y. Zhao, L. Yu, J. Xu, Y. Jiang, Y. Sheng, Y. Shi and K. Chen, *RSC Adv.*, 2017, **7**, 19457-19463.
80. D.-B. Li, L. Hu, Y. Xie, G. Niu, T. Liu, Y. Zhou, L. Gao, B. Yang and J. Tang, *ACS Photonics*, 2016, **3**, 2122-2128.
81. Y. Hou, X. Chen, S. Yang, Y. L. Zhong, C. Li, H. Zhao and H. G. Yang, *Nano Energy*, 2017, **36**, 102-109.
82. L. Zhu, Z. Shao, J. Ye, X. Zhang, X. Pan and S. Dai, *Chem. Commun.*, 2016, **52**, 970-973.
83. S. S. Shin, E. J. Yeom, W. S. Yang, S. Hur, M. G. Kim, J. Im, J. Seo, J. H. Noh and S. I. Seok, *Science*, 2017, **356**, 167-171.
84. L. Zhu, J. Ye, X. Zhang, H. Zheng, G. Liu, X. Pan and S. Dai, *J. Mater. Chem. A*, 2017, **5**, 3675-3682.
85. A. Bera, K. Wu, A. Sheikh, E. Alarousu, O. F. Mohammed and T. Wu, *J. Phys. Chem. C*, 2014, **118**, 28494-28501.
86. K. Wang, Y. Shi, W. Guo, X. Yu and T. Ma, *Electrochim. Acta*, 2014, **135**, 242-248.
87. S. S. Shin, W. S. Yang, J. H. Noh, J. H. Suk, N. J. Jeon, J. H. Park, J. S. Kim, W. M. Seong and S. I. Seok, *Nat. Commun.*, 2015, **6**, 7410.
88. X. Liu, C.-C. Chueh, Z. Zhu, S. B. Jo, Y. Sun and A. K.-Y. Jen, *J. Mater. Chem. A*, 2016, **4**, 15294-15301.
89. S. S. Mali, C. S. Shim, H. Kim and C. K. Hong, *J. Mater. Chem. A*, 2016, **4**, 12158-12169.
90. A. Bera, A. D. Sheikh, M. A. Haque, R. Bose, E. Alarousu, O. F. Mohammed and T. Wu, *ACS Appl. Mater. Interfaces*, 2015, **7**, 28404-28411.
91. S. S. Mali, C. S. Shim and C. K. Hong, *Sci. Rep.*, 2015, **5**, 11424.
92. K. Wojciechowski, T. Leijtens, S. Siprova, C. Schlueter, M. T. Hörantner, J. T.-W. Wang, C.-Z. Li, A. K.-Y. Jen, T.-L. Lee and H. J. Snaith, *J. Phys. Chem. Lett.*, 2015, **6**, 2399-2405.
93. W. Ke, D. Zhao, C. R. Grice, A. J. Cimaroli, J. Ge, H. Tao, H. Lei, G. Fang and Y. Yan, *J. Mater. Chem. A*, 2015, **3**, 17971-17976.
94. H. Yoon, S. M. Kang, J.-K. Lee and M. Choi, *Energy Environ. Sci.*, 2016, **9**, 2262-2266.
95. S. Ryu, J. Seo, S. S. Shin, Y. C. Kim, N. J. Jeon, J. H. Noh and S. I. Seok, *J. Mater. Chem. A*, 2015, **3**, 3271-3275.
96. Y. C. Wang, X. Li, L. Zhu, X. Liu, W. Zhang and J. Fang, *Adv. Energy Mater.*, 2017, **7**, 1701144.
97. C. Tao, S. Neutzner, L. Colella, S. Marras, A. R. S. Kandada, M. Gandini, M. De Bastiani, G. Pace, L. Manna and M. Caironi, *Energy Environ. Sci.*, 2015, **8**, 2365-2370.
98. J. Xie, X. Yu, J. Huang, X. Sun, Y. Zhang, Z. Yang, M. Lei, L. Xu, Z. Tang and C. Cui, *Adv. Sci.*, 2017, **4**, 1700018.
99. J. Lee, J. Kim, C. L. Lee, G. Kim, T. K. Kim, H. Back, S. Jung, K. Yu, S. Hong and S. Lee, *Adv. Energy Mater.*, 2017, **7**, 1700226.
100. T. Adhikari, M. Shahiduzzaman, K. Yamamoto, O. Lebel and J.-M. Nunzi, *Sol. Energy Mater. Sol. Cells*, 2017, **160**, 294-300.
101. Z. Zhu, J. Q. Xu, C. C. Chueh, H. Liu, Z. a. Li, X. Li, H. Chen and A. K. Y. Jen, *Adv. Mater.*, 2016, **28**, 10786-10793.
102. M. C. Beard, A. G. Midgett, M. C. Hanna, J. M. Luther, B. K. Hughes and A. J. Nozik, *Nano Lett.*, 2010, **10**, 3019-3027.
103. L. Wang, W. Fu, Z. Gu, C. Fan, X. Yang, H. Li and H. Chen, *J. Mater. Chem. C*, 2014, **2**, 9087-9090.
104. X. Zeng, T. Zhou, C. Leng, Z. Zang, M. Wang, W. Hu, X. Tang, S. Lu, L. Fang and M. Zhou, *J. Mater. Chem. A*, 2017, **5**, 17499-17505.

Journal Name

ARTICLE

Inorganic ESLs	SnO_2	ESL	preparation method	preparation temperature of ESL(°C)	perovskite layer	Champion PCE(%) on rigid susbtrate	Champion PCE(%) of Flexible PSC	Reference
		SnO_2	sol-gel & spin-coating	80	$(FAPbI_3)_{0.85}(MAPbBr_3)_{0.15}$	19.20	16.11	32
		SnO_2	spin-coating	180	$MAPbI_3$	17.21	N/A	33
		SnO_2	spin-coating & chemical bath deposition	180	$Cs_xFA_yMA_{1-x-y}Pb(I_zBr_{1-z})_3$	20.70	N/A	34
		a-SnO_2	chemical bath deposition	55	$MAPbI_3$	14.80	N/A	35
		SnO_2	electro-deposition technique	50	$MAPbI_3$	13.88	N/A	37
		SnO_2	plasma-enhanced atomic layer deposition	100	$MA_{0.7}FA_{0.3}PbI_3$	N/A	18.36	38
		Li-doped SnO_2	spin-coating	185	$MAPbI_3$	18.20	14.78	39
		SnO_2	spin-coating	200	$MAPbI_3$	13.00	N/A	40
		SnO_2	spin-coating	150	$(FAPbI_3)_{0.97}(MAPbBr_3)_{0.03}$	19.90	N/A	41
		Sb-doped SnO_2	oil bath & spin-coating	100	$MAPbI_3$	17.70	N/A	42
		SnO_2/graphene quantum dots	spin-coating	180	$MAPbI_3$	20.23	N/A	43
		Y-Doped SnO_2	hyrdrothermal reaction	95	$MAPbI_3$	17.29	N/A	44
		Nb-doped SnO_2	spin-coating	190	$(FAPbI_3)_{0.85}(MAPbBr_3)_{0.15}$	17.57	N/A	45
		MgO/SnO_2	spin-coating	200	$MAPbI_3$	18.82	N/A	46
		SnO_2/PCBM	spin-coating	185	$MAPbI_3$	19.12	N/A	47

		SnO_2/C60	spin-coating	140	$MAPbI_3$	15.18	N/A	48
	ZnO	ZnO	chemical bath deposition	90	$MAPbI_3$	8.90	2.62	49
		ZnO	electro-deposition technique	150	$MAPbI_3$	10.91	N/A	50
		ZnO	sol-gel & spin-coating	140	$MAPbI_3$	8.77	N/A	51
		ZnO	atomic layer deposition	80	$MAPbI_3$	16.50	N/A	52
		ZnO	precipitation method & spin-coating	65	$MAPbI_3$	15.70	10.2	53
		ZnO	precipitation method & spin-coating	60	$MAPbI_3$	14.00	N/A	55
		ZnO	precipitation method & spin-coating	120	$MAPbI_3$	8.73	4.29	56
		ZnO/SnO_2	spin-coating	200	$MAPbI_3$	14.00	N/A	57
		ZnO/PCBM	spin-coating	RT	$MAPbI_xCl_{3-x}$	16.80	N/A	59
	WO_x	WO_x-TiO_x	spin-coating	150	$MAPbI_3$	14.47	N/A	61
		WO_x	spin-coating	150	$MAPbI_xCl_{3-x}$	8.99	N/A	62
		W(Nb)O_x	spin-coating	120	$MAPbI_xCl_{3-x}$	N/A	15.65	63
		WO_x/C60	spin-coating	150	$MAPbI_3$	16.07	N/A	64
		WO_3	spin-coating	100	$MAPbI_xCl_{3-x}$	9.50	N/A	65
	Other oxides	CeO_x	sol-gel & spin-coating	150	$MAPbI_3$	17.04	N/A	66
		Nb_2O_5	e-beam evaporation	RT	$MA_{0.33}FA_{0.66}Pb(Br_{0.16}I_{0.84})_3$	18.59	15.56	68
		a-Nb_2O_5	radio frequency magnetron sputtering	RT	$MAPbI_3$	17.10	12.1	69
		Nb_2O_5	electrophoresis	RT	$MAPbI_3$	14.60	N/A	70
		In_2O_3	sol-gel & spin-coating	200	$MAPbI_3$	15.30	N/A	71

		In_2O_3/PCBM	sol-gel & spin-coating	200	$MAPbI_3$	14.83	N/A	72
	CdS	CdS	chemical bath deposition	60	$MAPbI_3$	10.80	N/A	73
		CdS	spin-coating	100	$MAPbI_3$	11.20	N/A	74
		CdS	chemical bath deposition	65	$MAPbI_3$	16.10	N/A	75
		CdS	thermal evaporation	RT	$MAPbI_3$	12.20	N/A	76
		CdS	homogeneous precipitation	90	$MAPbI_3$	2.27	N/A	77
		CdS	chemical bath deposition	72	$MAPbI_3$	15.10	N/A	78
		CdS	chemical bath deposition	85	$MAPbI_3$	14.68	9.9	79
	Bi_2S_3	Bi_2S_3	thermal evaporation	RT	$MAPbI_3$	13.10	N/A	80
	In_2S_3	In_2S_3	chemical bath deposition	100	$MAPbI_3$	18.22	N/A	81
	Zn_2SnO_4	Zn_2SnO_4	spin-coating	100	$MAPbI_3$	N/A	15.3	87
		Zn_2SnO_4	hyrdrothermal & spin-coating	180	$MA_xFA_{1-x}Pb(I_yBr_{1-y})_3$	17.70	11.4	88
		a: amorphous		RT: room temperature	MA: methylammonium FA: formamidinium			

Tab. 1 Preparation methods of inorganic ESLs and performances of resultant PSCs

Organic ESLs	Fullerene	ESL	preparation method	preparation temperature of ESL(°C)	perovskite layer	Champion PCE(%) on rigid susbtrate	Champion PCE(%) of Flexible PSC	Reference
		C60	spin-coating	60	$MAPbI_xCl_{3-x}$	13.50	N/A	92
		C60	thermal evaporation	RT	$MAPbI_3$	15.14	N/A	93

		C60	thermal evaporation	RT	$MAPbI_3$	19.12	16	94
		C60 pyrrolidine tris-acid	spin-coating	RT	$MAPbI_3$	18.39	17.04	96
		PCBM	spin-coating	RT	$MAPbI_xCl_{3-x}$	11.50	9.2	3
		PCBM	spin-coating	RT	$MAPbI_3$	15.30	11.1	95
		TiOx/PCBM	spin-coating	120	$MAPbI_3$	17.60	N/A	97
		PCBM:PCBDAN	spin-coating	100	$MAPbI_3$	18.10	14.2	98
		PCBM:PEI	printing	RT	$MAPbI_3$	17.30	N/A	99
	Non-fullerene	TiOx/PDI-glass	chemical bath deposition & spin-coating	150	$MAPbI_3$	5.75	N/A	100
		CDIN	spin-coating	80	$MAPbI_3$	17.10	14.2	101
				RT: room temperature	MA: methylammonium			

Tab. 2 Preparation methods of organic ESLs and performances of resultant PSCs

QDs ESLs	CdSe QDs	ESL	preparation method	preparation temperature of ESL(°C)	perovskite layer	Champion PCE(%) on rigid susbtrate	Champion PCE(%) of Flexible PSC	Reference
		CdSe QDs	hot-injection	140	$MAPbI_3$	11.70	N/A	103
		CdSe QDs/PCBM	spin-coating	RT	$MAPbI_xCl_{3-x}$	13.70	N/A	104
				RT: room temperature	MA: methylammonium			

Tab. 3 Preparation methods of QDs ESLs and performances of resultant PSCs